Advanced Energy Materials

ADVANCED ENERGY MATERIALS
www.advenergymat.de

RESEARCH ARTICLE OPEN ACCESS

Design Matters: How Cell Architecture Shapes the Performance, Cost, and Environmental Impact of Battery Technologies

Nicolas Peter Kaiser[1,2,3] | Florian Hölting[1,2,3,4] | Duc Minh Nguyen[1,2,3] | Martin Florian Börner[1,2,3] | Mark Junker[1,2,3,4] | Moritz Fabian Schütte[1,2,3] | Florian Ringbeck[1,2,3] | Dirk Uwe Sauer[1,2,3,4,5]

[1]Chair for Electrochemical Energy Conversion and Storage Systems, Institute for Power Electronics and Electrical Drives (ISEA), RWTH Aachen University, Aachen, Germany | [2]Center for Ageing, Reliability and Lifetime Prediction of Electrochemical and Power Electronic Systems (CARL), RWTH Aachen University, Aachen, Germany | [3]Juelich Aachen Research Alliance, JARA-Energy, Aachen, Germany | [4]Institute for Power Generation and Storage Systems (PGS), E.ON ERC, RWTH Aachen University, Aachen, Germany | [5]Helmholtz Institute Münster (HIMS), Jülich, Germany

Correspondence: Duc Minh Nguyen (batteries@isea.rwth-aachen.de)

Received: 30 September 2025 | **Revised:** 30 October 2025 | **Accepted:** 7 November 2025

Keywords: battery cell production | bottom-up modelling and trade-off analysis | battery cell design and performance comparison | battery cost analysis | life cycle assessment

ABSTRACT

The mounting demand for battery cells in the context of the energy transition necessitates evaluation methodologies that extend beyond mere performance metrics. This work presents a multidimensional framework that simultaneously integrates electrical performance, economic costs, and life cycle assessment into a consistent analysis of real and virtual cells. In total 140 cells were modeled, covering commercial chemistries and systematically permuted configurations. The framework enables systematic comparisons of real commercial cells and virtual redesigns by varying cell parameters under consistent boundary conditions without unintended side effects. Ultra high energy cells were generated, achieving very high energy densities under idealized design assumptions. Lithium-iron-phosphate (LFP) battery cells exhibit global warming potential values of $53-63\,kg\,CO_2$-EqkWh, while sodium-ion batteries (SiB) show a slightly higher range of $59-72\,kg\,CO_2$-EqkWh. Depending on housing and anode composition, production costs range from $32.7\,€/kWh$–$69.3\,€/kWh$ for LFP and $31.7\,€/kWh$–$82.4\,€/kWh$ for SiB. SiB cells achieve mineral resource scarcity values of about $5\,kg\,Cu$-EqkWh, three times lower than lithium-ion batteries. Cathode chemistry proves decisive for ecological performance, with nickel sulfate-based precursors showing the highest acidification values and LFP cells showing the lowest. Housing design plays an important role: pouch formats minimize costs and emissions. Systematic permutations show that increasing energy density is a key lever to lower environmental burdens.

1 | Introduction

The demand for batteries has significantly increased [1–3] due to the global transition toward renewable energy and the intensified electrification of the transportation sector. This development is closely linked to the goal of reducing CO_2 emissions and promoting sustainable energy solutions [4]. Batteries are central to this transformation, enabling both efficient energy storage and high-performance operation in electric vehicles and stationary systems [5, 6].

Nicolas Peter Kaiser and Florian Hölting contributed equally.

Additionally, the EU's digital battery passport will become mandatory on February 18, 2027. This regulation necessitates a thorough evaluation of battery cells, focusing on electrical performance, environmental impact, and economic considerations. The battery passport requires comprehensive documentation that covers performance parameters, carbon footprint assessments, and circularity metrics throughout the battery lifecycle. As a result, assessing batteries on multiple dimensions is no longer optional; it has become a compliance requirement [7, 8].

Moreover, recent publications have highlighted that sodium-ion batteries (SiBs) are emerging as a more affordable and environmentally friendly alternative to lithium-ion batteries (LiBs) [9–12]. This shift in focus emphasizes the growing interest in finding sustainable battery technologies that can meet the growing demand for energy storage while minimizing resource scarcity.

Given the significant variations in cell chemistry and design approaches [13] [14], facilitating a rapid evaluation of battery cells in terms of performance, cost, and environmental impact is essential. Battery design can differ among others by their chosen electrodes, housing dimension, and housing type, but also by their coating thickness, chosen electrolyte and so on. Various design parameters result in different electrical performances, as well as distinct ecological and economic impacts of the battery cell. A bottom-up cell design approach that focuses on battery components and their physical and chemical properties allows for the direct derivation of performance parameters from design specifications and material characteristics [15].

A broader scientific analysis of different battery technologies regarding their environmental and economic impacts has been conducted in the literature. However, only a few studies that consider all three dimensions - environmental, economic, and performance - could be identified. In Popien et al. [16], a comparison of various cell technologies at the battery pack level is carried out using the ecoinvent 3.8 [17] database as the environmental data source and the Battery Performance and Cost model (BatPaC) [18] for performance, production, and economic data. Additionally, Barke et al. [19] employ BatPaC as a data source to compare different battery technologies within a battery system designed for electric aircraft. An alternative approach to assess the performance of various batteries and analyze their mass composition for climate impact assessment is presented in Chordia et al. [20]. Furthermore, Degen et al. [21] utilize detailed bottom-up modeling of the analyzed battery cells, focusing on high-energy and high-power design approaches, and employ primary data from a battery cell factory to conduct an extensive environmental impact analysis spanning 18 different impact categories. Real production data is used as the input for electricity and heat demand. The assessed battery cells are virtual, so their performance in applications is unclear. Lastly, the influence of cell housing and specific cathode materials, such as lithium iron phosphate (LFP) or nickel manganese cobalt (NMC) was also investigated [22] [23].

However, a thorough analysis that jointly considers the electrical performance, ecological, and economic impacts of existing and permuted battery cell technologies has not yet been provided in the literature within a single framework. In particular, no life cycle assessment (LCA) exists that directly compares real, measured cells across such a broad set of designs. Furthermore, flexible models that can evaluate battery costs based on various cell and electrode designs are required [24]. This paper addresses this gap by enabling, for the first time, a systematic comparison of battery cells and by quantifying how design parameters such as housing type, coating thickness, or active material affect overall cell performance and sustainability. Moreover, we explicitly model the synthesis pathways of all active materials used in the investigated LiB and SiB chemistries. The precursor chemicals required for these syntheses serve as the actual inputs to the LCA, instead of relying on aggregated database values. Such a detailed and consistent representation of active material synthesis has not yet been carried out in any previous battery LCAs.

This paper introduces a comprehensive framework for evaluating the electrical performance, ecological impact, and economic implications of different battery cells with varying design parameters. It enables the analysis of the multi-dimensional effects of changes in housing type and dimensions, electrode configurations, and the coating thickness of the active material in battery cells. Such information is crucial for production decisions, as it highlights key metrics that influence the feasibility and sustainability of battery manufacturing processes. To achieve this, a bottom-up cell modeling tool is combined with a cell production and cost model. Additionally, an automated interface to an environmental impact assessment database is implemented within this study. Moreover, through the use of cell cost tool and ISEA Cell and Pack Designer (ICPD), it becomes possible to create virtual cells based on various design parameters that enable rapid evaluation of both costs and ecological impacts. By integrating these three components, the ISEA virtual cell framework is established, as presented in Figure 1.

To assess the analysis of various design parameters concerning electrical performance, as well as ecological and economic impact factors, a total of 140 battery cells with different design configurations were modeled and evaluated using the developed framework. The battery cell permutations are based on ten existing battery cells, referred to as the basis cells. Five different housing types - including cylindrical, prismatic, and pouch-bag housings - were employed to analyze the effects of housing variations on the basis cells. Additionally, different electrodes were combined with each other within the five housing types, featuring a specified high-energy coating design.

This paper is organized to first present the methodology of the virtual cell framework in Chapter 2. This includes the fundamentals of the bottom-up cell modeling tool and the modeled cells in Section 2.1, as well as the production and cost model in Section 2.2.1. Additionally, Section 2.3 discusses the automatic interface to an environmental impact assessment database and provides a brief introduction to the methodologies of LCA and life cycle inventory assessments (LCIA). The assessment methodology and the additional datasets for the LCA are detailed in Section 2.4.

Chapter 3 focuses on the results of the multi-dimensional analysis and comparison of the modeled cells. The electrical performance is analyzed in Section 3.1, while Section 3.2 investigates the costs and environmental impact of the analyzed cells. Additionally, Section 3.3 discusses the comparability of various battery cells,

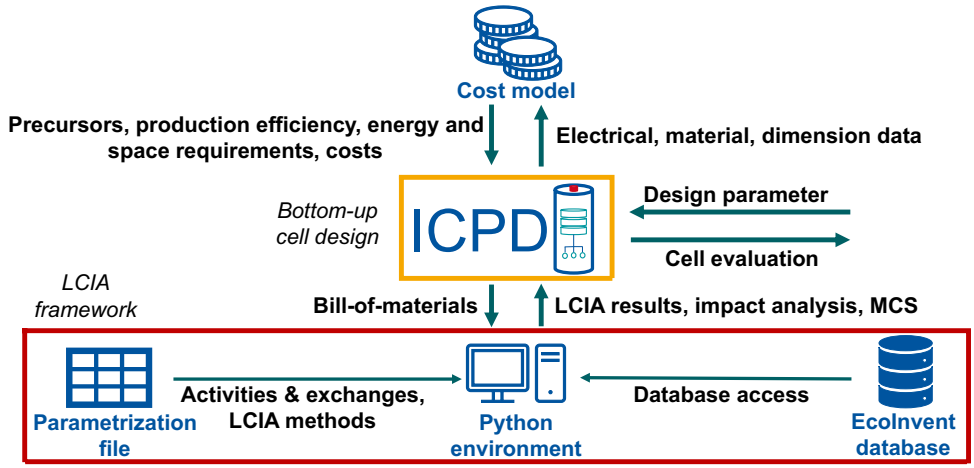

FIGURE 1 | Flow-chart of the ISEA virtual cell framework.

while Section 3.4 analyzes the impact of energy mix composition. Lastly, a brief conclusion is provided.

2 | Isea Virtual Cell Framework - Methodology

The battery cells, along with their material parameters and electrical performance, are calculated using an enhanced version of the ICPD developed by Kuipers et al. [15] and made open-source [25]. Section 2.1 details the modeling process and modeled cells within this study. To estimate battery cell costs, the ISEA-developed cost tool is used [26], including updated figures and additional chemistries, as described in Section 2.2. The LCIA utilizes a modified ecoinvent 3.11 database [17, 27], with Section 2.3 outlining the interface, parameterization, methods, and impact categories. Figure 1 illustrates the framework's flowchart and the interaction between the tools.

2.1 | Technical Bottom-Up Cell Modeling Using ICPD

A bottom-up cell design approach that focuses on battery components and their physical and chemical properties allows for the direct derivation of performance parameters from design specifications and material characteristics. This process effectively links material-level properties with cell-level performance. Only a few software solutions provide the advantages mentioned earlier. One noteworthy option is BatPaC, an open-source excel tool, developed by Argonne National Laboratory [18]. However, it has certain limitations that restrict analysis capabilities. These include non-modifiable open-circuit potentials (OCP), a reliance on default look-up tables for electrode balancing and open-circuit voltage (OCV) calculations, restricted access to the bill of materials (BOM) for the battery cell, and limited options for housing configurations.

Therefore, a by the institute of power electronics and electrical drives (ISEA) developed comprehensive cell modeling tool, the ICPD [15] [25], is used and adapted, providing the required complexity and flexibility. Comprehensive details about this tool can be found in Kuipers et al. [15] and an open-source repository [25]. The tool has been updated to include a graphical user interface for easier access.

2.1.1 | General Approach ICPD

The ICPD is a MATLAB tool for bottom-up battery cell modeling that employs an object-oriented approach. Each battery cell component is encapsulated as a class, allowing specific attributes and methods to characterize its properties. Components derive from the superclass *Material*. Higher-level components, such as electrode coatings, incorporate instances of *Binder*, *Conductive additive*, and *Active material* classes, reflecting the bottom-up formation of the coating. Creating a battery cell, an instance of the class *Cell*, requires instances of the *Electrode stack* and *Housing* classes, along with specifying the creation mode [15].

The *Electrode stack* consists of two *Electrode* objects representing the anode and cathode, along with a *Separator* and an *Electrolyte* object. Additionally, the creation mode must be specified. The electrode stack serves as the initial level of an electrochemical system, with balanced cell performance managed through its class methods. These methods are influenced by creation modes like *Standard*, *Fit surface capacity* and *Voltage Limit*.

In the *Standard* and *Voltage Limits* modes, the amount of cyclable transfer material - lithium or sodium - is determined based on the electrode containing the lesser amount. Consequently, the occupancy range of the more abundant electrode is adjusted to maintain balance while adhering to the OCP limits of each electrode. The OCV of charging and discharging, as well as the minimum and maximum voltage, are derived from these adjusted ranges. In *Standard* mode, no further adjustments are made to the stoichiometric window, and stack-specific parameters such as capacity, energy, minimum voltage, and maximum voltage are calculated accordingly.

In the *Voltage Limits* mode, datasheet-defined parameters for the voltage limits, are used to assess the stack's voltages. If a limit is breached, the ICPD attempts to align the target voltage setpoints with the calculated values by adjusting the electrodes' stoichiometric window while maintaining usable capacity. If

unsuccessful, the OCV is adjusted to comply with voltage limits, leading to modified occupancy ranges and reduced capacity.

Before the *Fit surface capacity* mode performs the same steps as the Voltage Limits mode, the surface capacities of both electrodes are equalized by reducing the thickness of the electrode with a higher capacity to match the other. This is particularly useful for creating balanced virtual cells without existing counterparts. Aforementioned stack parameters are calculated afterwards.

The *Cell* constructor operates in two modes: *standard-cell* and *FitStackToHousing*. In *standard-cell* mode, the electrode stack is not adapted to housing dimensions, while *FitStackToHousing* calculates the size of electrode coatings based on the housing type, determining the length and height of the electrode coatings, though not the thickness. During charging or discharging, the volume expansion of the electrode stack is modeled by a void space within the housing, especially relevant for electrodes containing silicon [28]. Additionally, the number of sheets required for pouch housings and the quantity of jelly rolls necessary for prismatic housings encompass both electrodes and separators are calculated. After adjusting the dimensions of the electrodes and separators, the electrode stack parameters are updated, followed by the calculation of cell-level parameters like weight, BOM, and energy density.

The ICPD includes a comprehensive database that features various materials and components, allowing for parameter studies, such as comparing different housing types - prismatic, cylindrical, and pouch bag - for specific battery cells. On the other hand, accurate electrical and material parameters rely on a thorough dataset, often obtained through post-mortem and teardown analyses [29–35]. These analyses involve opening the battery cell in an inert argon atmosphere to examine the individual components [36].

Material properties can also be sourced from the literature [15], including densities from databases like Materials Project [37]. The OCP of established and future active materials can be found in publications like in Andre et al. and Nitta et al. [38–40].

The ICPD offers a wide range of possibilities, such as comparing different cell chemistries within a single housing through virtual cell creation and parameter variation. However, there are limitations as well. The extensive data foundation required, along with the inherent measurement uncertainty, can lead to discrepancies between the properties measured in real cells and those calculated by the ICPD (see also Section 3.1). A more detailed explanation and comparison of the modeled and measured values can be found in Kuipers et al. [15].

2.1.2 | Modeled Cells Within This Study

This study utilizes data from both actual existing cells and individual components, such as housings and various electrodes, to conduct a comprehensive analysis. Three different groups of cells are modeled to assess the influence of the design parameters. First, the basis cells are derived from measurements of existing full cells. Based on these ten cells, variations are created using five different housings, resulting in a total of 50 different cell configurations. Additionally, 80 permutations are generated by combining the different anodes and cathodes of the basis cells with the five distinct housings, all while following a high-energy design approach.

Basis Cells

Table 1 presents the commercial basis cells used in this study, derived from battery cells that underwent post-mortem analysis by the ISEA and partially supplemented with data from the literature. Digital twins were created using voltage thresholds from the data sheets, with the *voltage limit* method used at the electrode stack level and the *standard-cell* method at the cell level. An evaluation of discrepancies at the cell level - between the available electrode stack dimensions and those calculated from post-mortem measurements - revealed no significant discrepancies.

The study encompasses a diverse array of battery technologies, including two types of battery cells with LFP cathodes, one with $Ni_{0.8}Mn_{0.1}Co_{0.1}O_2$ (NMC811) cathode - combined with a graphite-silicon blend with 3.5 % weight proportion of SiO (Si035C) for the anode - two cells featuring lithium-titanate oxide (LTO) anodes, one cell with a $Ni_{0.80}Co_{0.15}Al_{0.05}O_2$ (*NCA*) cathode, and one *SiB* equipped with an $Ni_{0.342}Mn_{0.325}Fe_{0.333}O_2$ (NMF) cathode and an hard carbon C_9 (HC) anode. The battery cells are available in three formats: prismatic, pouch, and cylindrical. Their capacities range from 2.69 *Ah* to 132.81 *Ah*, covering both high-power and high-energy options. This variety provides a representative overview of the different battery technologies included in this study.

Additionally, virtual basis cells (denoted with the prefix *v*) are considered in this study. These are either derived from post-mortem analyses of active materials — namely an NMC cathode with 92 % nickel, 3 % manganese, and 5 % cobalt content (NMC92), used as a cathode in *vNMC*2, and a C_6 anode with a 20 % weight fraction of silicon oxide (Si20C), used as a anode in *vCSi*. Or taken from the literature, adding a virtual cell with a lithium cobalt oxide (LCO) cathode and a C_6 anode and referred to as *vLCO* [41–45]. Based on the three additional active materials, three virtual basis cells were modeled: *vCSi*, *vLCO*, and *vNMC*2. The Tesla 4680 cylindrical housing was used, see also section housing variations, with the cell level creation mode set to *FitStackToHousing*.

The coating thicknesses for the *vCSi* and *vNMC*2 cells were set using the *Fit surface capacity* creation mode, based on laboratory measurements of the C_6+Si and NMC92 electrodes at 50 µm. The *vCSi* cathode uses NMC811, while the *vNMC*2 anode consists of graphite. The *vLCO* cell featured an LCO cathode at 50 µm and a graphite anode. The coating thicknesses were adjusted according to the surface capacity during the creation of the electrode stack. The full-cell voltages are based on the OCP limits of the electrodes specified in S1. As a result of including these additional electrodes, a diverse range of current electrodes is available in this work.

TABLE 1 | Bottom-up modeled commercial basis cells of this study with values calculated by the ICPD; *Data from datasheet.

Property	LFP1	LFP2	LTO1	LTO2	NMC1	NCA	SiB
Anode	C_6	C_6	LTO	LTO	C_6+3.5 %wt SiO	C_6	HC
Cathode	LFP	LFP	NMC622	NMC433	NMC811	NCA	NMF111
Type	Cylindrical	Prismatic	Pouch	Prismatic	Cylindrical	Cylindrical	Cylindrical
Weight g	68	3,176.67	277.96	548.52	47.43	47.11	85.71
Dimension mm	13 × 650	170 × 173 × 48	219 × 127 × 6	115 × 103 × 23	9 × 650	9 × 650	13 × 700
Capacity Ah	2.69	132.81	10.68	25.03	3.38	3.40	3.67
Energy Wh	8.76	436.69	25.57	57.43	12.13	12.61	10.28
Min. Voltage V	2	2.5	1.52	1.6	2.50	2.75	1.5
Max. Voltage V	3.6	3.8	2.8	2.7	4.2	4.2	3.95
Energy density Wh/kg	128.85	137.47	91.99	104.70	255.62	267.67	119.89
Power density W/kg*	2,600	1,250	1,559	1,818	742	482	609
Source	ISEA	ISEA	ISEA	ISEA	ISEA [46]	ISEA	ISEA [47–49]

Housing Variations

To investigate the influence of different battery housings on electrical, ecological, and economic factors, five additional housings have been modeled. The focus of the study is primarily on housing formats commonly used in vehicles, as well as on smaller representative formats. To begin with, the 4680 cylindrical housing, as used by Tesla, was modeled within the ICPD based on teardown data from Ank et al. [34] and Gorsch et al. [50]. As a smaller-scale alternative, a 21700 cylindrical housing, derived from ISEA teardown measurements, is utilized. When comparing the 21700 and 4680 cylindrical housings, it is notable that the wall thicknesses differ significantly. The wall thickness of the 21700 housing is 0.2 mm, while the 4680 housing has a thickness of 0.48 mm. This increase in thickness is necessary to provide the mechanical stability required for the larger 4680 housing. As a result, the weight-to-inner volume ratio of the 4680 is approximately 20 % higher than that of the 21700 housing. Additionally, the BYD blade 138*Ah* prismatic housing represents a large-scale prismatic option and was modeled in the ICPD using data from iEST [51] and Gorsch et al. [50]. Moreover, the minor adapted prismatic housing of the *LTO2* basis cell exemplifies a smaller prismatic option. For automotive applications, the pouch-bag housing of the VW ID3 from the 2020 version was modeled, with data sourced from Gunter et al. [52] and Wassiliadis et al. [53].

To obtain the housing variations, the electrode stacks of the basis cells are used as well as the presented housings and a cell is created by utilizing the *FitStackToHousing* creation mode.

Cell Permutations

To investigate the maximum achievable energy content, cell permutations are modeled using a (ultra)-high-energy approach. The coating thicknesses are set to typical values found in high-energy cells. Different anodes, such as C_6, C_6 + 3.5 % SiO, and C_6 + 20 % SiO, are paired with cathodes like LFP, NMC92, NMC811, NCA, and LCO across five housings, resulting in 80 unique combinations. The SiB cell's coating thickness is also adjusted, while the electrolyte - based on propylene carbonate, ethylene carbonate, and dimethyl carbonate as solvents -, current collector - cathode collector 13 µm and anode collector 11 µm thick -, and separator - 10 µm thick and equally based on polypropylene and polyethylene - remain consistent for all permutations. Only SiB permutations utilize aluminum for both anode and cathode current collectors. LTO cells are excluded to focus solely on high-energy configurations.

To achieve a high-energy design, the coating thickness of the lower gravimetric capacity electrode was set to 98 µm. The thickness of the electrode coating with the higher gravimetric capacity was then reduced using the *Fit surface capacity* mode to ensure a balanced surface capacity between both electrodes.

The coating thickness of 98 µm was determined by analyzing various teardowns of high-energy cells and calculating the average layer thickness from the thicker electrode. The cells analyzed included the following: the Tesla Model 3 pouch LFP compared to C_6 [33], the ID.3 pouch NMC compared to C_6 [52], the Tesla 4860 cylindrical NMC compared to C_6 [34], the BYD blade pouch LFP compared to C_6 [50], and the Samsung 48G cylindrical NMC compared to C_6 with silicon [54, 55].

Since no full-cell voltage limits are established for the cell configurations, the *Standard mode* is employed to create the electrode stacks. Additionally, to account for irreversible phase transitions, structural degradation, and plating that can occur due to overdischarging or overcharging specific active materials, the OCP limits of the active materials used are derived. This allows for an adjustment of the stoichiometric window accordingly. In the S1 is an overview of the OCP limits for each active material being considered. In all cases, the maximum possible OCP limits were chosen to ensure that no irreversible effects occur within the cell.

As a result, the generated permutations achieve broad voltage ranges, thick coatings, optimal space efficiency, and very high energy densities following the (ultra)-high-energy approach.

2.2 | Bottom-Up Battery Cell Cost modeling

In this section, we present the cost modeling framework used to evaluate the modeled cells. First, the existing cost model is described, including its underlying assumptions and data sources. Subsequently, the modifications and adaptations implemented for the present study are detailed.

2.2.1 | Existing Cost Model

This study adopts a bottom-up cell cost model based on previous work [26]. The model calculates costs and energy consumption in a battery factory using a bottom-up approach, estimating total costs under various scenarios and identifying key cost drivers. It incorporates cell parameters from ICPD to evaluate processing and material costs. The model uses input parameters like cell specifications, general technical, and economic parameters, and material costs. Cell specifications include electrical parameters like capacity and voltage, which determine the number of cells needed for the desired output. Additional cell design parameters are required to estimate the number of production machines. For example, electrode dimensions affect the number of coating machines.

In the cost tool, production steps are divided into three parts. First, the electrodes are prepared by mixing materials and coating them onto the current collectors. Initially, the coating process of the positive and negative electrodes is modeled using a wet process, widely used in the industry [56]. They are then compressed through a calendaring process. Next, they are cut into the desired sizes and undergo a vacuum drying process. The second step involves assembling the cells by stacking or winding the separator and electrode sheets. The assembled construct is inserted into specific cell housings and sealed. Finally, the cell is filled with electrolyte. In the last step, the manufactured cells undergo formation, ageing and end-of-line testing.

Costs and energy use are calculated for each process based on the manufacturing method. Floor space, labor, and investment costs are estimated from the number of machines.

Material costs are quantified by the required amount of material, considering rejection rates and the desired output capacity of the factory per year. Rejection rates vary by process, whereas overall equipment effectiveness is used to account for factors such as unplanned downtime in production. Precursor materials for the active materials are quantified by reaction equations of synthesis processes, which are described in Section 2.2.2. The production of precursor materials, electrolyte, and separator is not modeled and is assumed to be purchased. Since no price data for different electrolytes are available, the same price per kilogram was assumed for each electrolyte. Among anode materials, users can choose between pure or silicon-doped graphite and LTO. In contrast, the chemical composition of the cathode materials can be freely specified, as proposed by Greenwood et al. [57]. Additionally, to incorporate SiB, NMF was added as a cathode material, and HC was added as an anode material. The flexible approach allows for the easy implementation of new materials.

Various sources provide input parameters, including the ICPD, teardown analysis, literature, and databases. Material and component costs come from databases, exchanges, or literature. Production parameters are rarely available, so they are gathered from manufacturer websites, expert interviews, or literature. Most parameters are adopted from prior work, which details the bottom-up cost [26]. A complete list of parameters and assumptions is included in S2.

2.2.2 | Determination of the the Bill of Electrode Materials

To generate the input streams of raw materials, including their quantities for the BOM, the synthesis equations are used for the active materials. The initial step in this procedure involves determining the mass of the active material within the coating. This is achieved by incorporating the anode or cathode coating and subsequently multiplying by the respective active material share. The analysis accounts for double-sided coatings and material loss in production.

In the ICPD, lithium and sodium are categorized separately from the active material of the cathode as transfer materials. After the initial cycle, some of the transfer material remains within the electrodes. This residue is not cycled again and is therefore classified as inactive transfer material. Since all transfer material is included during the synthesis process, both active and inactive transfer materials are applied to the cathode active material. The total weight of these materials is now considered the output of the cathode synthesis. In contrast, because there is no transfer material in the anode before cycling, the output of the anode active materials is defined as the total weight of the anode active material within the cell.

The synthesis equations are divided into those for the cathode and those for the anode. Furthermore, a distinction is made between active materials for LiBs and SiBs. Initially, an evaluation of the components present in the active material is conducted to facilitate the selection of the appropriate synthesis route. The weight masses are determined using the molar masses and stoichiometry based on the reaction equations. In the context of this study, all reactions are regarded, incorporating both the initial streams and the subsequent by-products. The masses of the inputs and by-products are entered in the respective BOM. The mass of the by-products is recorded as a negative value and treated as waste emissions. The addition of ammonium hydroxide (NH_4OH) in co-precipitation syntheses of layered oxide cathode precursors is typically used as a pH-adjuster and complexing agent rather than as a stoichiometric reagent that forms a solid by-product. In practice, most of the NH_4^+ (and the water) remain in the liquid phase (filtrate) after precipitation of the metal hydroxide precursor; this filtrate is usually neutralized, washed, and in many cases recycled or returned into subsequent synthesis steps rather than being discharged as a permanent waste stream. Accordingly, it is reasonable in our LCA calculations to treat NH_3/NH_4^+ and H_2O from the pH control step as process-internal streams rather than as final waste emissions [58, 59].

In this study, the following cathode active materials for LiBs are analyzed: LFP, NMC, LCO, and NCA. Moreover, NMF will

be considered as the SiB cathode active material. The following materials are considered as anode active materials for LiBs: LTO, C_6, and C_6 mixed with silicon oxide (SiOx). All synthesis equations used are listed in the S1.

2.3 | Automatic LCIA Parametrization

For the automatic parametrization and calculation of the LCIA of different kinds of battery cells, the framework uses the open-source Python library brightway25 [60, 61]. As database ecoinvent version 3.11 is used.

An effective LCIA of a product necessitates comprehensive data on the materials used and their quantities. The ICPD, along with the presented cost modeling, including the synthesis of various anode and cathode materials, as well as the assessment of electricity, heat, and factory consumption, provides this data foundation. This results in five distinct BOMs that serve as inputs for the LCIA, as shown in Figure 1.

These BOMs include specifications for cell assembly, as well as individual components such as the anode, cathode, electrolyte, and separator. Notably, the BOM for cell assembly encompasses the quantities of specific anode, cathode, electrolyte, and separator materials required for the assembly process. Moreover, the materials utilized in the cell housing are accounted for, which include aluminum or stainless steel for the main structure, aluminum for the terminals, and polypropylene, which serves as the insulating layer in cylindrical or prismatic cell designs. Additionally, the energy inputs - electricity and heat - along with overall factory consumption, are integral components considered within the cell production process, thereby delineating the system boundaries of the cost model. The quantities no longer correspond exactly to those in the ICPD because they have been modified by the cost tool. The scrap rates described have been taken into account.

The BOM for both the anode and cathode primarily consists of the precursor materials used in the synthesis, along with the solvent, conductive additive, binder, and current collector. Additionally, any side products resulting from the synthesis are regarded as negative flows within the BOM. In response to the aforementioned descriptions, the BOMs of the separator and electrolyte are also generated and modified by the cost tool to take account of rejection rates.

Reference processes for battery cell components were created in the ecoinvent database using openLCA [62] and supplemented with transport processes from the NMC cell dataset. China was chosen as the production country, reflecting its 85 % market share in 2023 [63]. Each process was assigned an UUID and stored in an Excel mapping file. The Python workflow, based on the openlca2bw package [64], iteratively matches BOM entries to corresponding ecoinvent exchanges, scaled to 1 kg of cells, and added linked production or waste processes. This procedure was repeated for all five BOMs to generate a consistent battery production activity. Finally, the enriched database was imported into brightway25, which set up the characterization matrices for the LCIA calculations. To capture uncertainties in BOM-to-ecoinvent mapping, a Monte Carlo simulation (MCS) was applied. Each exchange was parameterized with uncertainty types and probability distributions (e.g., normal, log-normal, uniform) [65, 66]. MCS generates random values from these distributions across thousands of iterations, recalculating the LCA in each run [67]. This produces a range of possible outcomes rather than a single deterministic value. From these results, statistical measures such as mean, standard deviation, and confidence intervals are derived, enabling robust quantification of variability and supporting more reliable interpretation of environmental impacts [68, 69].

After calculating the static LCIA and conducting a MCS, a contribution analysis is performed based on the static LCIA results and the user-selected method and impact category combinations. This analysis allows for a detailed examination of the contributions made by each battery component, as well as the various flows within those components.

All results from the static LCIA, MCS, and contribution analysis are saved as Excel files on the file system. The ICPD then loads these results and saves them to the corresponding cell objects in the database after formatting. Additionally, the electricity, heat, and factory consumption impacts are reallocated to the five components based on the battery production information. The consumption data related to the production processes has been allocated to the cell assembling processes within the LCIA.

2.4 | LCA Conditions and Considerations

LCA provides a structured method to evaluate environmental impacts across a product's life cycle, considering material use, energy consumption, and waste generation [70, 71]. It supports sustainable decision-making by identifying optimization potentials. LCA consists of four phases: Goal and Scope Definition, which defines objectives, audience, and system boundaries [70]; Life Cycle Inventory (LCI), which collects input and output data such as energy, raw materials, and emissions [70]; LCIA, which evaluates results across categories like climate change and resource depletion [72, 73]; and Interpretation, where findings are synthesized into conclusions and recommendations [70].

2.4.1 | Scope of the Study

The scope of this LCA study is defined as "Cradle to Gate". This approach encompasses all stages of the life cycle from raw material extraction through production processes up to the point where the cells leave the factory gate. In this context, we analyze the environmental impacts associated with battery cell production, excluding subsequent use and end-of-life phases. This allows us to focus on the manufacturing processes and material inputs that significantly contribute to the overall environmental footprint of different battery technologies [74].

2.4.2 | Functional Unit

The functional unit of this LCA is defined as 1 kilowatt-hour (kWh) of energy content stored in the battery cells. This standardization enables a direct comparison between different types

of battery cells based on their energy output capacity, providing a common metric for evaluating their environmental performance.

2.4.3 | Impact Assessment Categories

In this assessment, several midpoint impact categories have been selected to evaluate the environmental implications of battery cell production. Midpoint indicators describe environmental impacts at an intermediate stage in the cause-effect chain (e.g., greenhouse gas emissions leading to climate change) and are commonly used in life cycle assessment due to their lower uncertainty compared to endpoint indicators [75, 76].

- **Global Warming Potential over 100 years (GWP)**: Measures the contribution to climate change by assessing greenhouse gas emissions. [kg CO_2-eq]
- **Cumulative Energy Demand (CED)**: Evaluates total energy consumption throughout the life cycle. [MJ]
- **Terrestrial Acidification Potential**: Assesses potential acidifying emissions that can harm terrestrial ecosystems. [kg SO_2-eq]
- **Mineral Resource Scarcity (MRS)**: Analyzes depletion of mineral resources used in battery production. [kg *Cu*-eq]

2.4.4 | Assessment Methodology

The assessment methodology utilized in this study is ReCiPe with the H-method. ReCiPe is a widely recognized framework for life cycle impact assessment that integrates various environmental impact categories into a comprehensive evaluation. The H-method refers specifically to the hierarchical approach within ReCiPe, which provides a balance between midpoint and endpoint indicators and facilitates clearer communication regarding trade-offs among different environmental impacts. [77] Among various impact assessment methods utilized in LCAs, ReCiPe stands out due to its comprehensive nature. It encompasses both midpoint indicators - such as GWP - and endpoint indicators related to human health and ecosystem quality. The flexibility provided by ReCiPe makes it suitable for diverse applications within LCAs; it allows for detailed analyzes of trade-offs between different environmental impacts while offering a structured approach to evaluating sustainability across multiple dimensions [73].

This structured approach ensures that our comparative analysis of different battery cell technologies is robust and reflective of their potential environmental consequences during production.

2.4.5 | Input Data

The input data for this study are derived from cell generation within the ICPD and are further processed by the cell cost tool. This ensures that processes such as the synthesis of active materials are accurately represented in the assessment. All datasets utilized in this analysis originate from the ecoinvent database version 3.11, employing a cutoff allocation method. This approach is suitable for a cradle-to-gate assessment as it focuses on the environmental impacts associated with material extraction and production processes up to the point where products leave the factory gate [71], thereby providing a clear picture of resource use and emissions during these initial life cycle stages. Additionally, several datasets have been independently modeled based on more recent literature data: nickel sulfate [78], cobalt sulfate [79], lithium carbonate [80], lithium hydroxide [80], and the Chinese grid mix. The low import percentage [81] indicates that electricity generation can be assumed to equal consumption. The electricity generation is composed of various energy sources derived from both renewable and fossil fuels [82].

Nickel sulfate is a key precursor for layered oxide cathode materials (e.g., NMC, NCA) [83]. Although it is often obtained as a by-product of cobalt sulfate production, this stream is typically of technical grade and does not meet the >99.9 % purity required for battery applications, as it contains impurities such as Fe, Cu, Zn, Mg, or Al [84–86]. Achieving battery-grade quality therefore requires extensive purification (e.g., ion exchange, solvent extraction, crystallization). To reflect this, we modeled nickel sulfate production directly from class 1 nickel and sulfuric acid, rather than using the ecoinvent market mix (≈90 % by by-product from cobalt sulfate). This results in higher LCA impacts but more accurately represents battery-grade nickel sulfate. The energy that is used in the production of the electrodes' active material is taken from the ecoinvent database modeled processes of the materials (LFP, NMC, NCA, C_6 and silicon-coated graphite) or from literature data (others). For all NMC compositions, the same energy within the production of the active material is assumed. HC is modeled with data from Wickerts et al. [87]. Furthermore, energy data used in the NMF cathode active material is taken from Degen et al. [21]. Julien et al. [88] shows the energy of synthesis of LTO anode active material. Electricity demand data for LCO synthesis comes from Dunn et al. [89] The heat demand of 6 kWh kg^{-1} refers to the furnace processes (drying, calcination, and sintering) in the synthesis of active materials, and therefore, between the heat demands of LFP and NMC synthesis. The solid-state synthesis of LCO has a comparable energy requirement to other oxide-based cathode materials as LTO, as it also requires high calcination temperatures (700 –900 °C, several hours) and upstream grinding processes. [90]

3 | Multi-Dimensional Comparison of Cell Technologies

In the following subsections, the results of the comprehensive study on various battery designs are evaluated and analyzed in multiple dimensions.

3.1 | Performance Analysis of Modeled Cells

Figure 2 shows the electrical performance of the three different groups of cells.

3.1.1 | Basis Cells

The weight distribution among the cell components is illustrated in Figure 2a. One key advantage of pouch housings over pris-

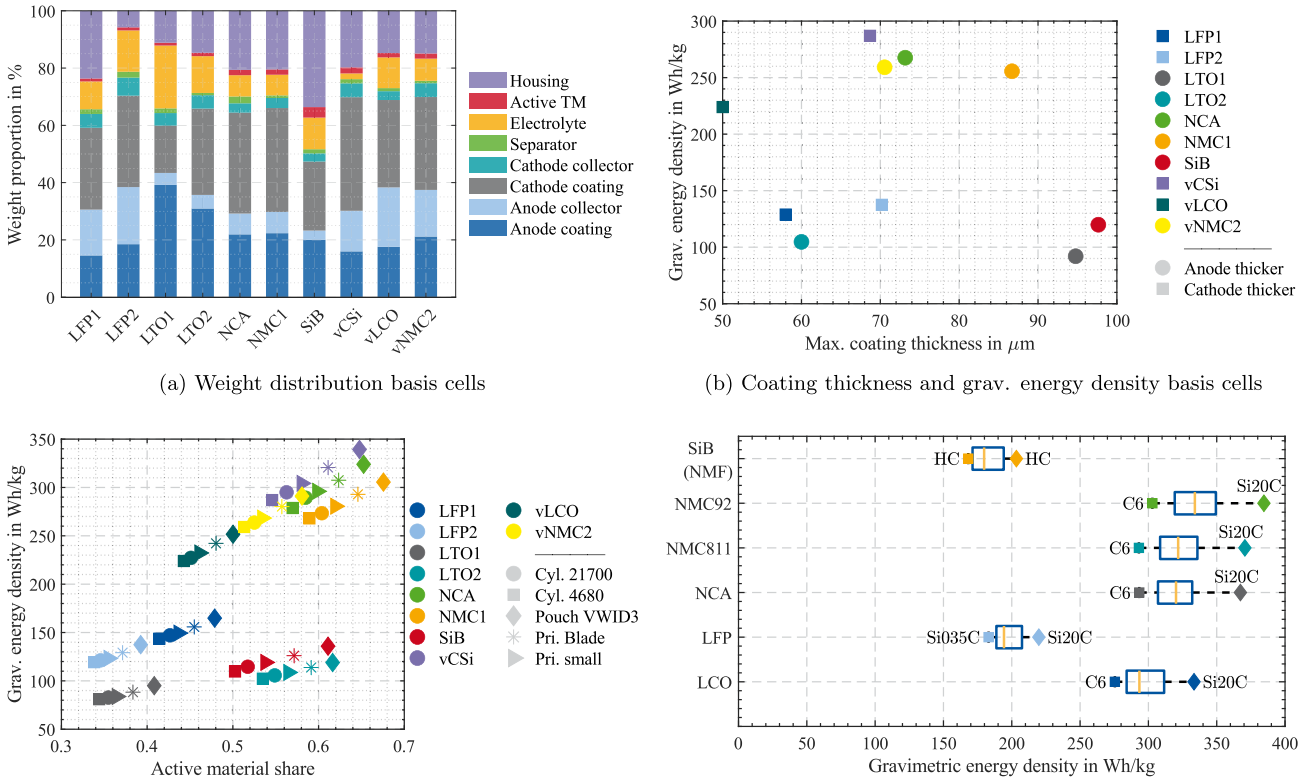

(a) Weight distribution basis cells

(b) Coating thickness and grav. energy density basis cells

(c) Active material share and grav. energy density of housing variations

(d) Distribution of the energy density of the cell permutations clustered by cathodes

FIGURE 2 | Electrical performance of basis cells, housing variations and cell permutations: Weight distribution of the cell components for basis cells (a) and grav. energy density versus coating thickness (b) as well as grav. energy density for housing variations (c) and cell permutations (d).

matic and cylindrical housings is their lower weight fraction. Additionally, large-format prismatic housings also result in a reduced weight fraction. Using anodes with a silicon-graphite blend can decrease the weight fraction of the anode. Furthermore, the higher molar mass of sodium contributes to a greater share of active transfer material in SiBs.

Figure 2b illustrates the coating thickness of the thicker electrode alongside the corresponding gravimetric energy density of the cells. Among the commercial basis cells, the *NCA* cell achieves the highest energy density, followed by the NMC cells. In contrast, the LTO cells and the SiB cell exhibit significantly lower energy densities. The coating of the cathodes is thicker only for the cells with LFP cathodes, which is due to the lower gravimetric capacity of LFP compared to graphite anodes.

As outlined in Section 2.1.1, the measured properties of the cells may deviate from those calculated within the ICPD framework. The average variation in capacity is 5.6 %, with the most significant discrepancy observed in the *SiB*, which exhibits a difference of 11.2 %. In the case of the *LFP*1, the calculated cell weight varies by 10.5 %, marking the highest noted difference; however, the average variation in weight is only 4.6 %. In addition, the discharge energy displays an average difference of 5.9 %, with the maximum variation recorded at 8.8 % for the *LTO*2. Gravimetric energy densities are generally overestimated for all cells except for the *SiB* and NMC1. Specifically, for *LFP*1, the deviation is 18.7 %, while the average deviation is 6.8 %.

The cell *vCSi* achieves among all basis cells the highest energy density of approximately 287 Wh kg^{-1}, thanks to its high silicon fraction, and it has a capacity of 24.2 *Ah*. However, the volumetric energy density is lower than that of the NCA cell due to the increased volume expansion of the silicon-graphite anode during lithiation.

The quality of the economic and ecological analysis of battery cells is closely linked to the data quality provided by the battery cell modeling framework. Therefore, it is essential to maintain low deviations in the main properties. The basis cells presented, modeled within the ICPD framework, demonstrate a relatively low deviation from the properties of their existing counterparts.

3.1.2 | Housing Variations

Figure 2c illustrates how these housing permutations affect gravimetric energy density and the share of active material based on the ten basis cells, resulting in a total of 50 cell permutations. Among the various configurations, the cylindrical housing demonstrates the lowest energy density. As expected, the 21700 housing outperforms the 4680 housing, as discussed in Section 2.1.2. Additionally, the pouch housing yields the highest energy density and the greatest share of active material across all cell groups, followed closely by the large-format prismatic Blade housing. In general, a greater share of active material - comprising both transfer material and the active components of both electrodes - correlates with a higher energy density.

When comparing the different cell technologies with various housings, it is noteworthy that the *SiB* achieves energy densities similar to those of *LFP*2.

3.1.3 | Permutations

Figure 2d displays the distribution of energy densities for cell permutations grouped by the cathode used. Generally, due to thicker coatings and varying combinations of housings and anodes, these permutations achieve higher energy densities compared to the basis cells. The combination of an *NMC92* cathode and a C_6 + 20 % SiO anode in a pouch housing attains the highest gravimetric energy density of 385 Wh kg^{-1}. However, this configuration does not yield the highest volumetric energy density due to significant volume expansion; the NMC92 combined with a C_6 anode achieves better volumetric density.

Overall, all electrode stacks housed in pouches outperform those in other housing types. For all cathode materials, the C_6 + 20 % SiO anode consistently outperforms other anode materials. In the case of cylindrical 4680 LFP cells, the C_6 + 3.5 % SiO anode exhibits the lowest energy density and a by 1 % slightly lower energy density compared to the C_6 anode variation, attributed to a slightly lower active material content of 49 % compared to 50 % for the C_6 anode and a lower nominal voltage due to a higher OCP at low lithiation-states of the silicon blend anode. The lower active material content arises from the lower surface capacity of LFP relative to other cathode materials, resulting in thinner anode coatings, particularly for the C_6 + 3.5 % SiO anode. The coating thickness is only 46.9 µm compared to 56.9 µm for the C_6 anode, which leads to a greater weight share of the current collector as inactive material in the anode's overall weight that can not be equalized by the higher gravimetric capacity of the anode material.

3.2 | Analysis of the Cost and Environmental Impact

The following subsections present an analysis of the cost and environmental impact of the basis cells, the housing variations, and the permutations.

3.2.1 | Investigation of Basis Cells

The results for the basis cells are shown in Figure 3 and subsequently analyzed. In the figures, red whiskers indicate the Monte Carlo uncertainty of the respective LCA results. Their length represents the variation in the results obtained from stochastic sampling. The magnitude of these whiskers depends on both the absolute value of the underlying impact category and the number of different process providers that are combined along the pathway to the final cell, with larger impacts and a higher diversity of providers generally resulting in wider uncertainty ranges. The detailed stochastic deviations are provided in an Excel file in the S2.

Global Warming Potential

Figure 3a shows the GWP of ten battery cell types, ranging from 64 *kg* CO_2-Eq for *vCSi* to 196 *kg* CO_2-Eq for *LTO*1. LTO cells have the highest GWP per kWh due to their low energy density and design for high-power applications. This requires more material for one kWh, resulting in higher emissions compared to other chemistries. Additionally, LTO cells have a low surface capacity, leading to a higher proportion of anode material to reach the cathode's capacity. Because LTO has a high operating potential and a lower specific capacity than graphite, LTO-based cells require more anode mass to balance a given cathode, and at the same discharge capacity and cathode loading deliver less energy due to the reduced average cell voltage.

Cells with layered oxide cathodes, such as NCA and NMC, have superior GWP performance due to their high energy density. Since high energy density requires less material per kWh, the emissions profile is more favorable. Among NMC-based cells, adding silicon to the anode (as in the NMC1 cell) reduces anode-related GWP further. Silicon-containing anodes have a higher surface capacity than graphite-only anodes and allow for thinner layers with the same capacity. This reduces the material demand and consequently the emissions related to the anode per kWh, despite the potentially higher energy requirement for silicon processing.

The *vNMC*2 cell, whose cathode consists of 92 *wt.*% nickel and 5 *wt.*% cobalt, also has a reduced GWP as well. Cobalt is a key driver of GWP due to the CO_2-intensive processes involved in its mining and refining. The *vNMC*2 composition substantially decreases the cobalt content while maintaining a high nickel content. This maintains high energy density while substantially lowering the GWP associated with the cathode.

Despite its higher energy density compared to LFP cells, the *vLCO* cell ranks second-to-last to LTO in terms of GWP per kWh. The primary reason is the high concentration of cobalt in its cathode. Cobalt extraction and refining are associated with high greenhouse gas emissions and dominate the environmental profile of LCO cells. Cobalt oxide is accountable for 47 % of GWP emissions resulting in 43 *kg* CO_2-Eq.

All LiB cells with nickel content below 60 % utilize lithium carbonate (Li_2CO_3), which is modeled in this study as being exclusively sourced from spodumene - a hard rock lithium ore. While both lithium carbonate and lithium hydroxide (LiOH) can be produced from spodumene, the production of 1 *kg* Li_2CO_3 generally requires slightly more spodumene than the production of 1 kg LiOH. In contrast, NMC cells modeled with LiOH benefit from a slightly lower spodumene demand per functional unit and reduced CED, contributing to a lower GWP (see Figure 3d).

With the exception of LTO and SiB, the contribution of cell assembly to overall GWP remains relatively minor. This is because most emissions are related to producing active material precursors, especially those involving transition metals, such as cobalt and nickel. The assembly-related GWP per kWh decreases as cell energy density increases because higher energy density cells require less ancillary material per kWh, such as casing,

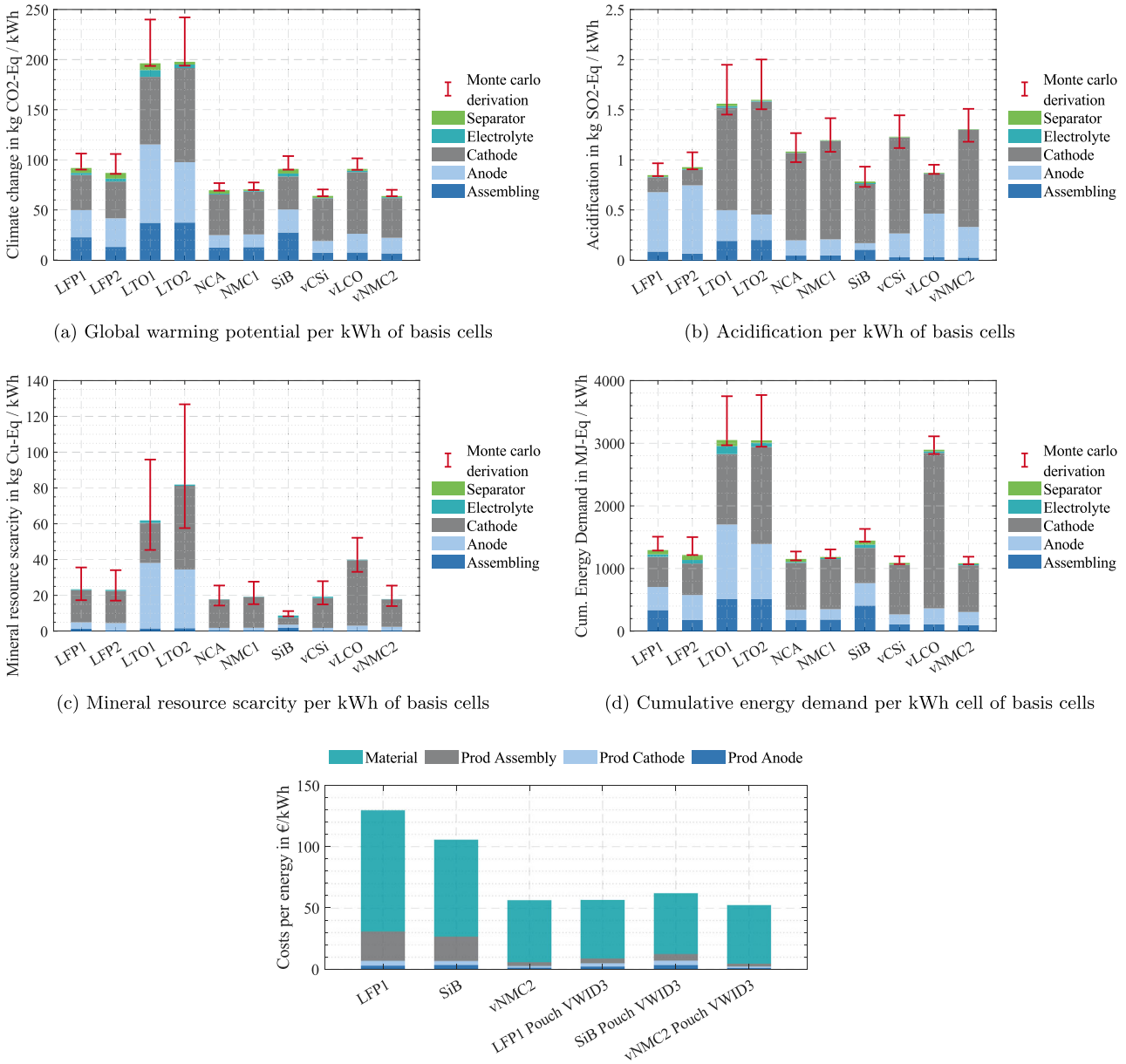

(a) Global warming potential per kWh of basis cells

(b) Acidification per kWh of basis cells

(c) Mineral resource scarcity per kWh of basis cells

(d) Cumulative energy demand per kWh cell of basis cells

(e) Manufacturing costs per kWh cell of basis cells; A&F stands for assembling and cell finishing

FIGURE 3 | Multi-dimensional evaluation of the basis cells. Global warming potential (a), acidification potential (b), mineral resource scarcity (c), cumulative energy demand (d) and manufacturing costs (e).

separators, and connectors, per unit of stored energy. For low-energy-density cells, such as LTO, the amount of inactive material and energy in production per kWh is significant; thus, the assembly stage contributes a larger proportion to the total GWP. Compared to other production countries the carbon intensity of the chinese grid mix is relativly high (0.626 *kg* CO_2-eq / kWh).

The GWP of SiB cell is similar to that of LFP cells, primarily due to their low energy density. Although the raw materials used in SiB cells generally have a lower environmental impact than those used in lithium- and cobalt-based batteries, the lower energy density of SiB cells requires a greater quantity of materials to achieve the same energy storage capacity.

The GWP contribution of the electrolyte and separator is comparatively low across all cell configurations and generally scales with the energy density of the cell. In low-energy-density cells such as *LTO*1, for instance, the electrolyte and separator each contribute approximately 3% to the total GWP. Within the electrolyte composition, dimethyl carbonate (DMC) accounts for the largest share of emissions, due to its comparatively high production-related carbon footprint.

In summary, variation in GWP among different cell chemistries is primarily determined by the raw material supply chain, particularly the production of cathode materials and achievable cell energy density. A high share of cobalt significantly increases

the GWP. The GWP values for layered oxide cells (e.g., NMC and NCA) in this study are largely in line with those reported by Degen et al. [21]. For example, comparing the GWP of NMC811 from ecoinvent with the value for our NMC811 cathode material (used e.g., in NMC1 cell) shows no significant differences, indicating that our modeled synthesis closely resembles the database process. In particular, our LFP configurations show an approximately one-third lower GWP compared to their results. This can be attributed to the higher energy densities achieved in our study through optimized cell designs, which allow for more energy to be stored per mass and reduce the relative impact of passive materials. The GWP results of the *SiB* are slightly higher in our study compared to those reported by [87], which can be attributed to the assumed production location in China. The higher carbon intensity of the Chinese electricity grid leads to increased emissions during energy-intensive manufacturing steps, while [87] consider a European production context with a significantly lower emission factor for electricity.

Acidification

Acidification in LCA is predominantly driven by emissions of sulfur dioxide (SO_2) and ammonia (NH_3), which contribute significantly depending on the cell chemistry and component design. Acidification results of basis cells are presented in Figure 3b. The acidification values vary between 0.78 (*SiB*) and 1.6 $kgSO_2 - Eq./kWh$ (*LTO*2).

For virtual cells such as *vLCO*, *vNMC*2, and *vSiC*, a crucial factor is the increased thickness of anode current collectors compared to baseline cells. In particular, for the *vLCO* cell, 46 % of the overall acidification impact arises from the smelting process associated with the anode collector. Additionally, 38 % of the acidification for *vLCO* stems from cobalt oxide used in the cathode; notably, only oxides are used as precursors rather than sulfates, which results in a comparatively lower acidification potential. In NMC-based cathodes, nickel sulfate plays a dominant role, particularly in the NMC1 variant, where it constitutes 73 % of the impact contribution, and the entire cathode accounts for up to 81 % of the acidification potential. Both cobalt sulfate and manganese sulfate are also key contributors within this share. For LFP cells, the *LFP*2 anode demonstrates a higher acidification impact due to a 5 µm thicker current collector compared to *LFP*1. In *LFP*1, 63 % of the acidification effect is attributed to the copper collector foil. In the synthesis of layered oxides (NMC, NCA, NMF), the NH_3 formed during the precipitation step does not leave the process but remains in the system and is reused as NH_4OH in subsequent reactions, thereby preventing emissions that would otherwise contribute to acidification. Concerning LCO cells, acidification potential is considerably lower compared to NMC cells, as no sulfates serve as precursors; instead, cobalt oxide is used. Due to the lack of nickel oxide in available datasets, nickel sulfate was used for modeling, slightly overestimating the resulting acidification.

For *SiB*, acidification levels are lower compared to NMC cells for two main reasons: (i) the nickel share in the active material is only about one third, resulting in significantly reduced use of nickel sulfate, which is a major contributor to acidification, and (ii) aluminum is employed as the current collector, thereby avoiding the acidification-related emissions associated with copper smelting. LTO cells display characteristic differences: *LTO*2 in particular exhibits a higher acidification potential of the cathode compared to *LTO*1, not primarily due to the cobalt content - which increases the acidification impact per kilogram of cathode material by only 11.3 % but due to the significantly higher share of cathode active material in the overall cell mass. This is a result of the lower gravimetric capacity of the *LTO*2 cathode coating (188 Ah kg^{-1}) compared to that of *LTO*1 (253 Ah kg^{-1}), which leads to a greater quantity of cathode material required per kWh. Consequently, the cathode active material fraction increases from 17.1 % in *LTO*1 to 28.3 % in *LTO*2, resulting in a higher acidification potential for the *LTO*2 cathode. On a per-kg basis, LTO anodes produce less acidification compared to other cells, since aluminum is used as the current collector, thereby omitting smelting processes that typically drive acidification. Titanium dioxide, used as a precursor for LTO anodes, is uncritical with respect to acidification. Lastly, when comparing *LTO*1 and *LTO*2 assemblies, acidification in *LTO*1 is larger relative to energy density, further highlighting the significance of cell design and component choice on the acidification footprint in battery production.

With regard to acidification potential, the impact of the electrolyte and separator is minimal, contributing less than 1 % combined. Acidification effects are largely driven by upstream emissions from metal extraction and processing, particularly for nickel, cobalt, and manganese. The acidification results of layered oxide cathodes containing nickel sulfate (NMC, NCA, and NMF) are approximately twice as high in this study compared to study from Degen et al. [21]. This difference arises from the modeling of nickel sulfate: instead of using the ecoinvent market mix, which largely represents by-product streams from cobalt sulfate production (≈90 %) and does not meet battery-grade purity requirements (see Section 2.4), we modeled nickel sulfate production directly from class 1 nickel metal and sulfuric acid. The market mix underestimates emissions because only a small fraction of the environmental burdens of nickel production is allocated to the by-product stream, whereas the remaining burdens are attributed to the primary cobalt production. Consequently, the acidification potential is significantly higher in our approach (0.45 kg SO_2 eq./kg $NiSO_4$) compared to the market mix (0.07 kg SO_2 eq./kg $NiSO_4$), reflecting the full process impacts of producing battery-grade nickel sulfate necessary for cathode synthesis. The choice of cathode precursors and the specific modeling of the synthesis pathways further influence the acidification scores. This highlights the strong influence of synthesis pathways on acidification impacts in battery production.

Mineral Resource Scarcity

Figure 3c shows the MRS, quantified in kilograms of copper-equivalent (Cu-eq). The MRS indicator in ReCiPe 2016 is defined as the Surplus Ore Potential (SOP). It quantifies the additional amount of ore that must be mined in the future due to today's extraction of one kilogram of a given mineral resource, expressed relative to copper as a reference.

Among the evaluated battery chemistries, *SiB* has the lowest material depletion potential because they do not require lithium,

cobalt, or nickel. These elements are categorized as more critical or scarce than sodium and iron [91]. Consequently, SiB cells have a markedly lower MRS score than LiB. The most decisive factor influencing the MRS of the evaluated cell types is the lithium source used in each chemistry. As previously described, all lithium-ion cells with a nickel content below 60 % - including *LFP*1, *LFP*2, *LTO*2, and *vLCO* - utilize lithium carbonate (Li_2CO_3), which is modeled in this study as being exclusively derived from spodumene obtained through hard rock mining. This extraction route is particularly resource-intensive and has a critical impact on the MRS score: for these cell types, spodumene-based lithium accounts for approximately 70 % of the total MRS. In contrast, the other layered oxide cells as *NCA* and NMC cells with a nickel content above 60 % use lithium hydroxide (LiOH), which is also modeled as being spodumene-based. However, its production requires slightly less spodumene per kilogram of lithium compound [80], resulting in a lower contribution of lithium to the overall MRS. For these cells, spodumene-based lithium accounts for only about 50 % of the total MRS because other materials as cobalt and nickel, contribute as well. Thus, differences in lithium compounds and associated resource efficiency represent the largest single contributor to MRS and account for the significant variation in MRS results among the evaluated lithium-ion battery technologies.

NMC cells with reduced cobalt content also achieve low MRS values due to their high energy density and reduced reliance on scarce cobalt. The *vNMC*2 cell (with less than 5 % cobalt) shows a comparable MRS to other NMC variants with higher cobalt content (e.g., NMC1). While the reduction in cobalt - a key driver of MRS - would typically lower the MRS, this effect is offset by the very high nickel content of the *vNMC*2 cathode (92 %), as nickel is also considered critical in terms of resource availability. In contrast, a higher manganese content would be beneficial for the MRS, since manganese is significantly less scarce compared to cobalt and nickel [92]. As a result, the overall MRS of *vNMC*2 remains on a similar level to that of other NMC chemistries. The *LTO*2 cell has a particularly high MRS for the cathode because it contains a significant amount of cobalt (about 35 %), which places it among the highest in terms of resource depletion impact.

Most anodes, primarily composed of graphite, show negligible MRS values since graphite is currently considered a noncritical raw material that is widely available. However, LTO anodes demonstrate slightly higher MRS values due to the inclusion of titanium. Cells with anodes that consists of graphite and silicon (e.g., NMC1 and *vCSi*) have slightly lower anode MRS values because a higher surface capacity allows for thinner anode layers per kWh. This decreases the total amount of material required for the anode.

The impact of cell assembly is negligible in all cases since the energy used for manufacturing (in the form of electricity and heat) involves minimal use of critical raw materials. For LCO cells, the high cobalt content in the cathode leads to a correspondingly high MRS score, reflecting the scarcity and country concentration risk associated with cobalt supply [91]. The lithium content in LFP cells is responsible for their significant MRS impact because lithium is considered a critical raw material with an increasing supply risk due to growing global demand [92]. In terms of MRS, electrolyte and separator contributions are likewise below 1 %. The MRS score is primarily determined by the demand for critical raw materials, especially lithium, cobalt, and natural graphite. Consequently, variations in cathode and anode compositions have a significantly larger influence on resource scarcity than supporting components such as the electrolyte or separator. MRS values are of similar magnitude compared to Degen et al. [21], but tend to be slightly lower in our study. This difference arises from the explicit modeling of lithium mining and refining processes, which were incorporated directly into our inventory instead of relying on generic ecoinvent upstream datasets. The detailed representation of spodumene-based lithium carbonate production leads to lower resource depletion indicators in our framework.

Cumulative Energy Demand

Figure 3d shows the CED results in megajoules per kWh (MJ/kWh) for the ten basis cells. The analysis shows that *LTO*1, *LTO*2, and *vLCO* cells have substantially higher CED values than other technologies. LTO cells demonstrate the highest energy demand, primarily due to their low energy density, which requires significantly more material per kWh of stored energy. For *LTO*2 specifically, the cathode fraction dominates the total CED due to its high cobalt content (approximately 35 %). Cobalt mining and refining are notably energy-intensive processes, requiring substantial electricity and thermal energy inputs throughout extraction and purification [91].

Despite their different material compositions and energy densities, LFP, NMC, NCA, and SiB cells demonstrate comparable CED values (approximately $1100 - 1200\,MJ - Eq/kWh$). LFP cells have lower energy density and thus require more material per kWh; however, they benefit from the less energy-intensive extraction and processing of iron and phosphate compared to the nickel and cobalt used in NMC and NCA cathodes. The *vNMC*2 cell, with its reduced cobalt content (5 %), has a slight advantage in terms of energy demand compared to standard NMC compositions. The high proportion of LCO cathode is striking. 84 % of the total energy requirement is caused by cathode production. Cobalt oxide accounts for as much as 76 % of the CED ($2206\,MJ - Eq$) due to the energy-intensive mining and processing process. Cells with silicon anodes (NMC1 and *vCSi*) have the smallest anode contribution to overall CED. This advantage stems from silicon's higher specific capacity, which enables thinner electrode layers and consequently reduces material requirements per kWh.

Conversely, *SiB* have a higher anode-related energy demand because their hard carbon anodes are derived from phenolic resins through energy-intensive production processes. For LiBs, natural graphite is considered as the anode material; if synthetic graphite were assumed instead, the CED impacts would be substantially higher. For CED, however, the relative impact of the electrolyte and separator is more pronounced. Depending on the specific cell configuration, their combined contribution can reach up to 7 % of the total CED (*LTO*1). This is due to the energy-intensive production processes of certain electrolyte solvents as DMC and polymer separator materials (polypropylene and polyethylene). CED results also show a comparable order of magnitude to those reported by Degen et al. [21] The consistency

between the two studies indicates that energy demands for material production and cell manufacturing are robust across different LCA methodologies. Minor deviations can be attributed to differences in the modeling of production processes, particularly in terms of energy supply and process efficiencies applied in the respective inventories.

Costs

The total manufacturing cost per energy of each basis cell in Figure 3e is divided into cost components consisting of material costs and production costs, which are further separated into each electrode, and the final cell assembly and finishing (A&F) (e.g., formation) of the battery cell.

Notably, precursor raw materials estimated by the synthesis for active material are included in the material costs. The largest portion of the total costs is for material costs with at least 66 %, followed by A&F, and electrode production. Among electrode production, anode and cathode production contribute similarly to the total costs, which are minor compared to the other costs above. LTO cells are the most costly technology with up to 133 $€/kWh$ followed by *LFP*1 with 98.69 $€/kWh$. *SiB* and NMC1 are around 79 $€/kWh$ and *vNMC*2 with cost of 51 $€/kWh$. *vLCO* amounts to costs of 58 $€/kWh$. Ultimately, *LFP*2 and *vCSi* have the lowest costs at 52 $€/kWh$ and 48 $€/kWh$, respectively.

Among material costs, expenses for raw materials, followed by passive components like housings and current collectors, make up the largest shares (see S1). The highest investment of over 60 % in active materials is found in LTO cells, which use expensive raw materials both on the anode and cathode side. On the anode side, lithium titanate oxide is used, while the cathode can include costly nickel or cobalt materials such as in LCO, NCA, or NMC. Additionally, LTO cells are designed for high-power applications, resulting in lower energy density and relatively higher costs per kWh. Anode material costs tend to be higher with hard carbon and lithium titanate oxide, as seen in *SiB* or LTO cells, compared to graphite and silicon-doped graphite. When comparing cathode materials, nickel-based cells exhibit higher material costs. Another major contributor to high material costs is the combination of cells with low stored energy per cell. Especially for *LFP*1 and *SiB*, these cells are less competitive than nickel-based options. High energy density results in low material costs per kWh, especially by reducing the amount of inactive material (such as housings, separators etc.). Additionally, large cells have advantages in same purchase parts such as housings and contacts. Both effects can be observed by comparing *LFP*1 and *LFP*2. The former can store about 50 times more energy, leading to significantly lower housing costs per kWh. High energy content is also evident in *vCSi*, *vLCO*, and *vNMC*2, supporting this observation.

Next, current collectors also significantly contribute to material costs. Their size and volume determine the cost of the current collectors. Aluminum is used exclusively on the cathode side, while anode current collectors are usually made of copper. However, in the case of LTO or SiB, aluminum can be used as an anode current collector, resulting in much lower costs. Therefore, the high costs of current collectors in LFP cells cannot be offset by their cheaper cathode materials compared to nickel-based cells. Nickel-based cathode cells have cathode materials that are twice as expensive, but this is balanced by their nearly double gravimetric energy density, resulting in lower active material costs for NMC cells compared to LFP cells.

A&F costs account for up to 80 % in the battery production. The highest assembly costs are found for cells with comparatively low energy, as this determines the number of annually produced cells, which in turn determines the required machines to fulfill the cycle time available in each process. In particular, assembly processes benefit from a lower number of cells that need to be processed for the same factory output in terms of GWh per year. Also, the number of electrical cycling devices used in formation and end-of-line testing can be greatly reduced by increasing the energy per cell. Formation and initial cycles are the most cost-intensive manufacturing steps, which account for almost 50 % of total A&F costs. Even though cycling currents increase, this results in significant cost reductions. The influence of cell capacity is evident in the distinct A&F costs between *LFP*1 and *LFP*2, which occur due to the low capacity and energy of the former cell. Similarly, *vCSi*, *vLCO*, and *vNMC*2 have low formation costs due to high stored energy, supporting the previous observations.

Besides formation and aging processes, another contributor is the stacking or winding of the electrode stack or jelly roll. Additionally, costs are proportional to the number and size of electrodes required for a given energy. Here, the highest costs are observed for the cylindrical format with rather low energy, as for *LFP*1, *NCA*, NMC1, and *SiB*.

Regarding the contact welding of cells, this process only occurs for pouch and prismatic battery types. Cylindrical cells are going through this process if a tabless design is used, which is not the case for the presented basis cells. The higher energy content of cells can decrease contact welding costs.

The electrolyte filling process has a rather small impact on assembly costs, accounting for less than 5 % of overall production costs. The final End-Of-Line check is affected by cell capacity and energy, similarly to processes in the formation. Housing assembly depends on cell capacity and energy, as more cells and thus more housing need to be fitted for a given factory output. Therefore, process cycle times are short and must be fulfilled by more machines, which leads to higher investment costs for both machines and factory building.

Compared to A&F, electrode production makes up between 4 % and 11 % of the total manufacturing costs. As mentioned, material costs are not considered here. In contrast, the mixing and coating processes have the highest share within the electrode production. The mixing processes, either for the anode or cathode, depend on the number of mixing machines, which increases with the volume of slurry needed per kWh. Therefore, electrodes that are capable of storing more energy per material exhibit cost advantages. The other processes during electrode production (coating, drying, calandering, and slitting) are roll-to-roll processes. The cycle time of these processes depends on the roll-to-roll speed. Therefore, the electrode area per kWh is the driving factor

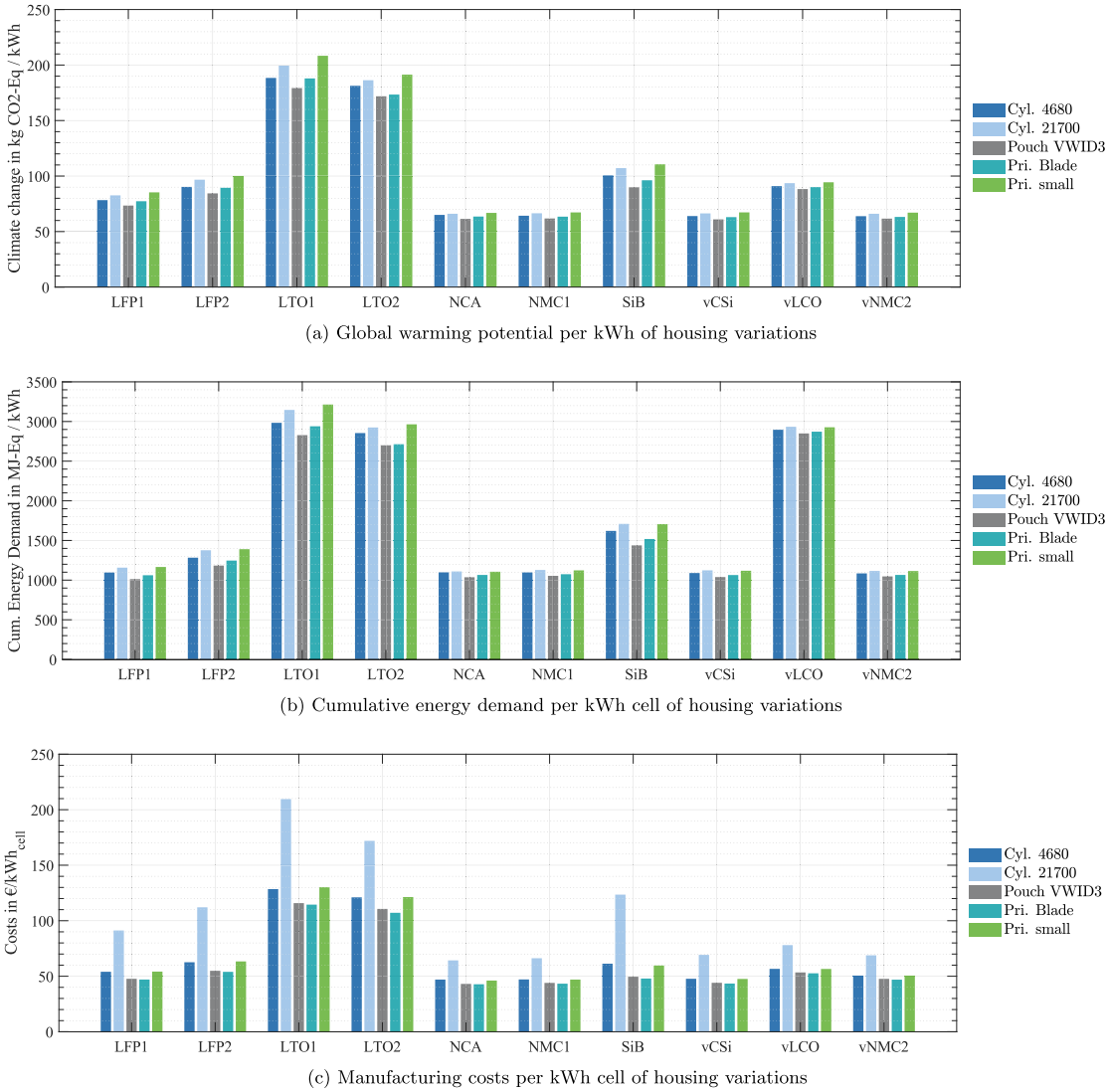

FIGURE 4 | Multi-dimensional evaluation of the housing variations. Global warming potential (a), cumulative energy demand (b) and manufacturing costs (c).

determining the required number of machines. Cells with thicker coating or higher energy density per active material volume show cost advantages in these production steps.

3.3 | Influence of Different Housing Types

This Section analyzes the influence of different housing types on GWP, CED and costs. Analyses and figures for acidification and MRS can be found in the S1.

Global Warming Potential

Figure 4a illustrates the influence of various housing types on GWP. The VWID3 pouch-bag housing achieves the lowest GWP due to its superior energy density and optimized active material composition (compare Section 3.1). It reduces GWP per kWh for most cell configurations. While the VWID3 provides a 3.5 % gain in energy density over the 4680, this advantage does not offset the greater emissions and energy consumption tied to aluminum housings compared to steel options.

In terms of GWP modification, the ascending sequence is led by the VWID3, followed by the Blade, cylindrical 4680, cylindrical 21700, and compact prismatic housing. Differences in energy density are less pronounced within the cylindrical and prismatic small group, creating a disconnect between energy density rankings and GWP scores. The prismatic small cell exhibits the highest GWP alteration due to its aluminum casing, while the 21700 assembly results in greater energy consumption than the 4680, as illustrated in Figure 4b.

The most prominent effects of the housing variations were observed in the *SiB* variations at approximately 19 %, followed by the LTO and LFP cells. These effects were particularly accentuated in cells with low energy densities. Conversely, the impact on GWP for high-energy density cells was minimal, staying below 10 %, due to the reduced influence of the assembly process related to the housing, as illustrated in Figure 3a.

Cumulative Energy Demand

Figure 4b depicts the alteration of the CED based on the housing variations. Variation of the housing leads to an alteration of the CED score by a maximum of 23 %. The *vLCO* variations show a small impact with 3 % corresponding to the low assembling share and high total CED score of the basis cell to be seen in Figure 3d.

Commonly, the pouch VWID3-housing is used as the baseline due to the lowest CED value. Whereby, aluminum-based housings have a higher CED score, due to a more energy-intensive production process of aluminum alloy, compared to steel-based housings. Therefore, for the variations of the basis cells for which the energy densities of the small housing and the cylindrical housings are closer together, the prismatic small aluminum housing leads to the highest alteration.

The differences in the assembly process based on the housing type have a smaller impact on the consumption of electricity, heat, and chemicals in the factory. However, the higher proportion of active materials in the Blade and VWID3 housings is significantly more important.

Costs

The influence of each housing type on the cost is visualized in Figure 4c. Lowest manufacturing costs of high-energy cells in Pouch VWID3 and Prismatic Blade housings range from 43 $€/kWh$ for high nickel-based cells and 55 $€/kWh$ for *LFP*2 cells, whereas high-power cells, such as LTO, have at least twice the cost. In contrast, using 21700 housings can raise costs by at least 47 %, for the *vNMC*2, up to 157 % for the *SiB*, respectively. As observed for the basis cells, material costs account for the majority of the costs.

Among cells with the same chemistry, the material cost structure remains mostly unchanged. The explanations for the cost deviations between different chemistries due to the used materials remain consistent with those provided in Section 3.2.1. However, an exception is observed for cells with 21700 housings, which incur substantial cost burdens due to housing expenses. Smaller housings accommodate less active material and consequently store less energy. Therefore, more cells are necessary to achieve a predetermined output in a battery manufacturing facility, increasing costs per kWh.

LFP and SiB cells with their comparatively low energy density require more passive cell components (housings, separators, etc.) per kWh. The costs of the housing are assumed to scale based on their weight, but also contain a fixed cost portion that penalizes small housing formats, where the processing costs in housing manufacturing have a larger share compared to material costs. This makes the cell chemistries with low energy densities (SiB and LFP) especially sensitive to changes in the housing format. Furthermore, an increased quantity of cells to be produced considerably raises the formation costs, as seen in the S1. The cost variations associated with anode and cathode manufacturing, resulting from housing modifications, exert only a minimal influence on overall expenditures. These costs are affected by the volume of cell production and the quantity of coating material applied to current collectors.

By comparing *LFP*1 and *LFP*2, the impact of housing variation becomes obvious. Nearly a 49 % cost reduction can be achieved for *LFP*1 when using Prismatic Blade housings instead of cylindrical 21700. Notably, *LFP*1 becomes less expensive than *LFP*2. Applying the same housing diminishes the significant cost advantage of basis *LFP*2 over basis *LFP*1 (see Figure 3e). This also accounts for *SiB* cells, which achieve tremendous cost reductions by applying a different housing. Nonetheless, LiB technologies show little cost advantage over *SiB*. These observations emphasize the pitfalls of comparing cells with different specifications or designs.

By integrating cell technologies and chemistries into the same housings, reliable cost comparisons become possible. The active material chosen determines the energy density of the cells and is a key factor influencing cost. Coating thickness also impacts the cell design, particularly regarding current collectors. The housing material itself has a minor impact, but its size is significant. Larger volumes enable greater energy storage and reduce costs, making the strategy of cell manufacturers shifting toward bigger cells more understandable.

3.4 | Analysis of Cell Permutation

The results of the permutations are presented in Figure 5 and further analyzed.

Global Warming Potential

The results of the battery cell permutations are presented in a boxplot. It is noteworthy that the GWP values for all new cell configurations are slightly lower than those of the Basis cells. This can be attributed to the fact that all cells have been designed as ultra high-energy cells with increased layer thicknesses. As a result, the impacts per kWh are significantly reduced because energy density increases, allowing more energy to be stored in the cell while decreasing the share of passive material.

The lowest GWP value is achieved by a cell with an NMC92 cathode and a Si20C anode. The Si20C anode provides a high gravimetric capacity, resulting in a very high energy density of approximately 380 Wh per kg, which substantially reduces the material demand per kWh and consequently lowers the GWP. For instance, NCA achieves a reduction of approximately 10 $kg\,CO_2 - Eq$ compared to the Basis cell, reaching a value of 59 $kg\,CO_2 - Eq/kWh$. Other layered oxide cells can also experience similar reductions by around this amount. In contrast, LFP can see its GWP reduced by approximately one-third, due to a significant increase in energy density resulting from its design as a high-energy cell. These values are comparable to those from Degen et al. [21] The lowest GWP values are achieved with the VWID3 pouch housing, primarily due to its minimal mass contribution to the overall weight of the cell. In contrast, the highest GWP values occur with prismatic small housings made from aluminum, which are energy-intensive to manufacture and thus generate higher emissions. The proportion of housing in total emissions

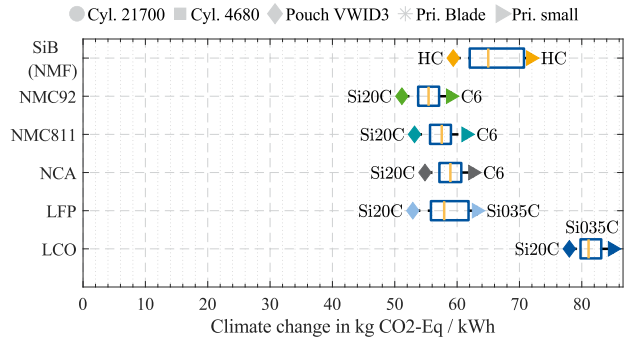

(a) Global warming potential per kWh of cell permutation clustered by cathode

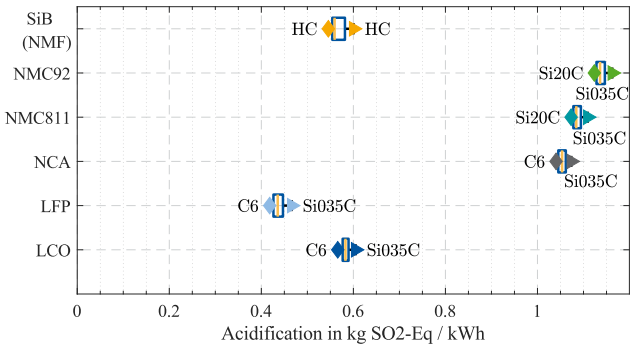

(b) Acidification per kWh of cell permutation clustered by cathode

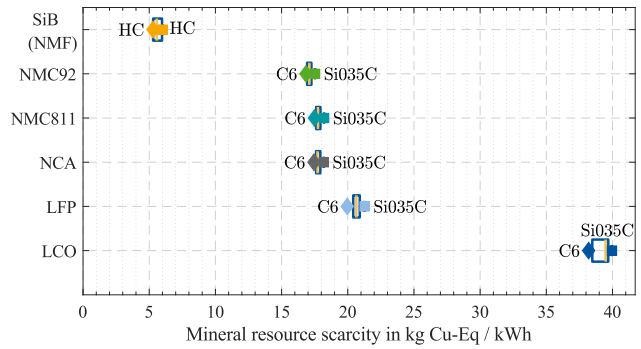

(c) Mineral resource scarcity per kWh of cell permutation clustered by cathode

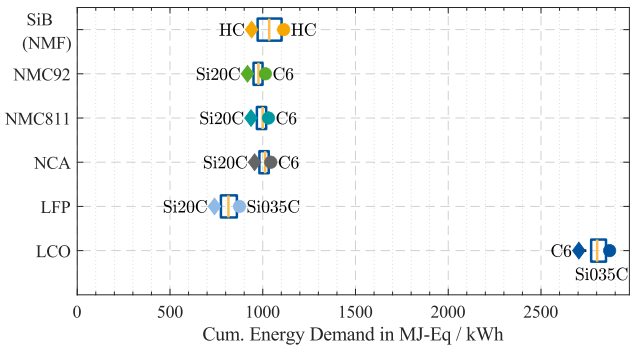

(d) Cumulative energy demand per kWh cell of cell permutation clustered by cathode

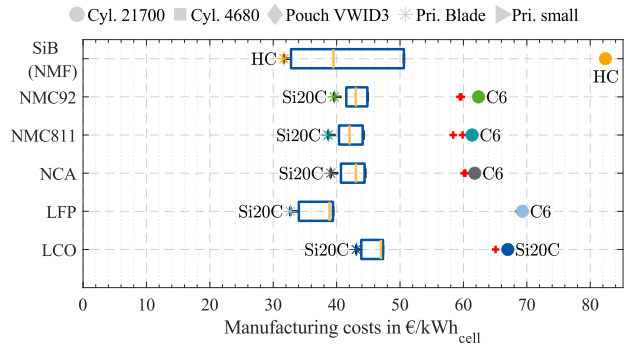

(e) Manufacturing costs per kWh cell of cell permutation clustered by cathode

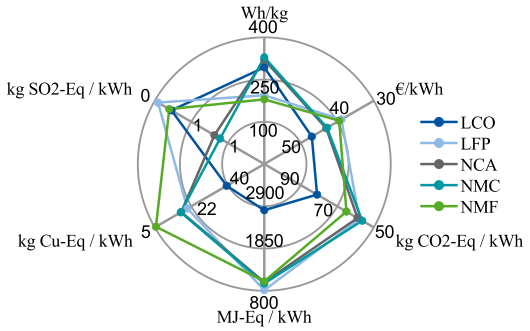

(f) Multi-dimensional comparison of cell permutations

FIGURE 5 | Multi-dimensional evaluation of cell permutation clustered by cathode. Global warming potential (a), acidification potential (b), mineral resource scarcity (c), cumulative energy demand (d), manufacturing costs (e) and multi dimensional comparison (f).

increases since more smaller cells must be produced per kWh compared to prismatic Blade housings. For all cells, an increase in anode capacity, such as through a 20 % silicon content on the anode within graphite, leads to a reduction in GWP. The higher energy density of these cells results in a decrease in GWP per kWh. For LFP and LCO, a lower silicon content (e.g., 3.5 %*Si*) results in an increased GWP. This occurs because the proportion of silicon relative to the active material increases, leading to a rise in GWP.

In summary, adding silicon to the anode is technically only beneficial when the cathode does not serve as the limiting electrode regarding surface capacity. Additionally, SiB cells also demonstrate reduced GWP through alternative housing material choices.

Acidification

The acidification potential of the evaluated battery cell permutations is shown in Figure 5b. Overall, the acidification values are on a similar level as those of the Basis cells, reflecting the comparable material composition and sourcing strategies. Across all housing formats, the pouch-type housing VWID3 consistently exhibits the lowest acidification values per kg of cell mass, primarily due to its minimal housing weight. However, when normalized

per kWh, pouch cells show the lowest acidification values, as their high energy density effectively reduces the relative impact of housing and inactive components. In contrast, prismatic small cells, featuring heavier aluminum-based enclosures, have lower acidification values per kilogram but higher values per kWh, as more cells are required to store the same amount of energy.

With regard to cathode chemistry, cells based on layered oxides synthesized from sulfate precursors, particularly NMC, NMF, and NCA variants, show the highest acidification values. This is attributed to the synthesis routes based on sulfate for nickel, manganese, cobalt, and aluminum, which release significant amounts of sulfur-containing emissions. In contrast, LCO cathodes, produced exclusively from oxide-based precursors, result in substantially lower acidification impacts.

On the anode side, the current collector plays a more significant role in acidification than the active material coating itself. While silicon increases the gravimetric capacity of the electrode, it also reduces the coating thickness, leading to a higher relative share of current collector material. This effect outweighs the gains in energy density, particularly for LFP and LTO cells, where silicon causes overly thin electrodes and boosts the share of inactive components. Consequently, cells with pure graphite anodes exhibit the lowest acidification, while the highest values occur at 3.5 % Si. This can be explained by the fact that a small Si addition does not sufficiently increase the energy density to compensate for the additional acidification burden of silicon. In contrast, at 20 % Si the higher energy density partly offsets the Si-related impacts, resulting in intermediate AP values. For NMC-based cells, the pouch variant with $Si_{20}C$ shows the lowest acidification value, although it is only about less than 1 % lower than the corresponding pouch cell with a pure graphite (C_6) anode. The values therefore lie very close together, which may be explained by the broader range of energy densities across all permutations (see Figure 2d) compared to NCA-based cells.

In summary, low acidification values are achieved through a combination of oxide-based cathode precursors, graphite-only anodes, and high-energy-density designs, particularly when using lightweight housings such as pouch formats.

Mineral Resource Scarcity

The MRS of the permuted battery cells indicates that the impacts are somewhat lower compared to the Basis cells; however, they do not differ significantly. The thicker layer thicknesses of the new cell configurations require more materials, which is reflected in the MRS values. These increased material demands are compensated by the higher energy density observed in the results per kWh. The lowest MRS values are obtained with the pouch VW ID.3 housing in all cells. However, the deviation compared to the Blade housing is very small, typically below 0.5 %, and can therefore be regarded as negligible. The Blade housing, which is made of aluminum, also achieves low MRS values due to the reduced share of passive materials. Particularly critical is the copper foil (anode current collector), whose proportion decreases in larger cells due to the overhang of anodes.

The generally low MRS values of the pouch VW ID3 housing can be attributed to its comparatively low material demand relative to other housing designs, which reduces the share of passive materials and thus the contribution to the overall MRS indicator. In contrast, cylindrical housings like the 4680 made of steel exhibit the highest MRS values. This is due to copper being added during steel production, which elevates the MRS. Additionally, for SiB architecture, the 21700 round cell housing shows the highest MRS as well. Although less housing material is required here, there is an increase in the active material content (such as nickel), which raises the MRS accordingly. Interestingly, the MRS results for the 4680 housing differ by only about 2 % from those of the 21700 round cell housing.

The lowest MRS values are obtained without silicon, while the highest values occur at 3.5 % Si addition. At this moderate share, the absolute input of Si material is already relevant, but the increase in energy density is not sufficient to reduce the indicator on a per kWh basis. In contrast, for 20 % Si, the higher energy density partially offsets the additional Si demand, resulting in intermediate MRS values between the Si-free and 3.5 % Si cases. Overall, the SiB architecture remains favorable regarding MRS in all types of housing because it does not use lithium. In comparison, LCO has a seven times higher MRS due to Li_2CO_3 and its high cobalt content.

Cumulative Energy Demand

The CED values for the evaluated battery cell permutations are shown in Figure 5d. Similar to the trends observed for GWP, the CED values are generally slightly lower compared to the Basis cells. This reduction is primarily due to the higher energy density of all evaluated configurations, which enables more efficient use of materials per kWh. In terms of housing formats, the pouch-type VWID3 configuration exhibits the lowest CED, driven by its low housing mass and high energy density. In contrast, the 21700 cylindrical cell exhibits the highest CED. This is due to the comparatively large share of steel in the housing relative to the total cell, which is particularly pronounced because this cell type stores the least energy per unit. Additionally, the pouch format requires approximately four times less housing material than the 21700 cylindrical design, further reducing its contribution to CED.

Among cathode chemistries, LFP exhibits the lowest CED values, as it relies on iron phosphate rather than layered oxide systems such as NMC and NCA, which incorporate energy-intensive materials like nickel and cobalt whose extraction is particularly energy demanding. Within the layered oxides, NCA shows slightly higher CED values compared to NMC due to the additional use of aluminum, which is also energy intensive in its production. At the other end of the spectrum, LCO cells exhibit the highest CED values by far, consistent with findings discussed in Section 3.2.1.

The anode material also plays an important role in the overall CED. For SiB, the use of polymer-based resins introduces a non-negligible energy demand. Depending on the housing configuration, the anode accounts for approximately 23-28 % of the total CED - ranging from 23 % for the 21700 steel-housed baseline cell to up to 28 % for the high-energy VWID3 pouch cell.

The effect of silicon additions to the graphite anode varies depending on the cathode chemistry. In layered oxide cells such as NMC811, NMC92, and *NCA*, the CED slightly decreases with silicon content due to the improved energy density and thinner anode coatings. However, in other chemistries, silicon increases CED because the energy-intensive production of silicon precursors outweighs the density benefit, particularly when it leads to thinner electrodes and a larger share of passive components (*vLCO*). The differences in CED between silicon-containing and pure C_6 anodes remain relatively small. For example, for the NMC811 pouch cell, the CED for Si20C and C_6 anodes vary only 3 % despite differences in energy densities (358 vs. 336$Whkg^{-1}$). These findings highlight that minor design variations can significantly impact the balance, underscoring the sensitivity of energy demand to both material and architectural parameters.

Costs

Figure 5e depicts the manufacturing costs per kWh of the permutations. The overall impact of cell chemistry, housing design, and capacity on cost structures remains significant and consistent with the trends shown for the Basis cells (see Section 3.2.1) and in the analysis of the housing variations (see Section 3.2.2). For the permutations (ultra)-high-energy cells have been created, resulting in lower costs when compared to the Basis cells. Especially, the combinations with silicon-doped anodes achieve higher capacities and therefore outperform cells with graphite anodes. Among all cell types, *SiB* and LFP chemistries exhibit the most significant cost variations. As discussed before, their low energy density makes them especially sensitive to design parameter variations. The lowest and highest costs are observed with *SiB*, ranging from approximately 32 €/kWh to 82 €/kWh. In terms of LiBs, LFP cells have the lowest costs at 33 €/kWh. However, LFP can also lead to costs as high as 69 €/kWh, underlying the importance of optimized cell design and giving the reason for the increasing size of LFP-based batteries in recent years. Costs among nickel-based LiB cells are similar, ranging from 38 €/kWh to 40 €/kWh when considering only Blade Housings. However, NMC92 incurs higher costs than NMC811 despite having a reduced cobalt content. Nonetheless, the lower cobalt usage does not offset the increased coating weight by 25 %, which raises costs for the cathode material. LCO cells show the minimal achievable costs at 43 €/kWh.

Across different housing types with consistent active materials on both the anode and cathode sides, a similar rank among housings is found as in Section 3.2.2. The most cost-effective cells can be achieved using Blade and Pouch VWID3 formats. In contrast, 21700 cylindrical formats remain the most expensive. Between these extremes, 4680 cylindrical and prismatic small housings are slightly more costly than the cheapest options. Independent of the chosen cathode material, the amount of passive material required per kWh decreases with increasing energy density. Therefore, high shares of silicon in the anode consistently show the lowest costs per kWh. Besides material costs, the increase in energy density reduces processing costs, since less material needs to be handled in the production of the anode, and fewer cells have to be processed during A&F. The adoption of silicon-doped anodes, which increases cells energy content, further emphasizes their cost-optimizing advantage.

Multi-Dimensional Comparison

Figure 5f illustrates the cell permutation clustered by five cathodes - NMCs cathodes are accumulated -, focusing on energy density, costs, and four impact categories of the LCIA. The median values for all permutations of each clustered cathode are utilized.

It is important to note that no clustered cathode can be considered the best for every category, highlighting the conflicting objectives involved in selecting the right cathode during the battery design process.

When comparing LFP batteries to SiB, which is represented by the NMF cathode, it is evident that SiB can achieve similar cost values but only higher GWP values. One significant advantage of the NMF cathode is its low material scarcity score, which is nearly one-third of that of the second-lowest score NMC. Additionally, LFP cells have a lower and in general, the lowest potential for acidification.

LCO cells clearly perform the worst in four out of six categories, indicating an outdated design. They only achieve good values in terms of energy density and acidification potential. Moreover, they are unrivaled in terms of volumetric energy density, which explains their continued use in mobile phones. This underlines that LCO technology still holds relevance for specific applications despite its overall unfavorable environmental profile.

Conversely, NCA and NMC cells exhibit similar figures across all categories, indicating a comparable chemical composition.

3.5 | Comparability of Different Battery Technologies

Numerous studies comparing different battery technologies often incorporate cells designed with varying approaches. This can create issues, particularly when ranking battery cells without accounting for the diverse design parameters.

This study examines how design parameters affect key metrics of different battery types. Figure 6 illustrates the impact of excluding housing effects on the material and total costs per kWh for *LFP1*, *SiB*, and *vNMC2* cells. *vNMC2* is the most cost-effective option when evaluating the basis cells alone based on their material costs, followed by *SiB* and *LFP*. This suggests that NMC cells offer a lower material cost per kWh compared to SiB and LFP cells. The significant role of housing costs is highlighted in the graph's purple sections.

In the right section of Figure 6a, material costs for the three cells fitted into the same housing - the pouch VWID3 - are shown, allowing for a more meaningful comparison. Here, *vNMC2* is more expensive than the *LFP* and *SiB*, while *SiB* emerges as the most economical choice, invalidating previous conclusions based solely on basis cell comparisons.

Considering production costs as shown in Figure 6b changes the ranking of the most economical cells. While the order of the basis cells remains the same, the total costs for the *LFP1* cell are now

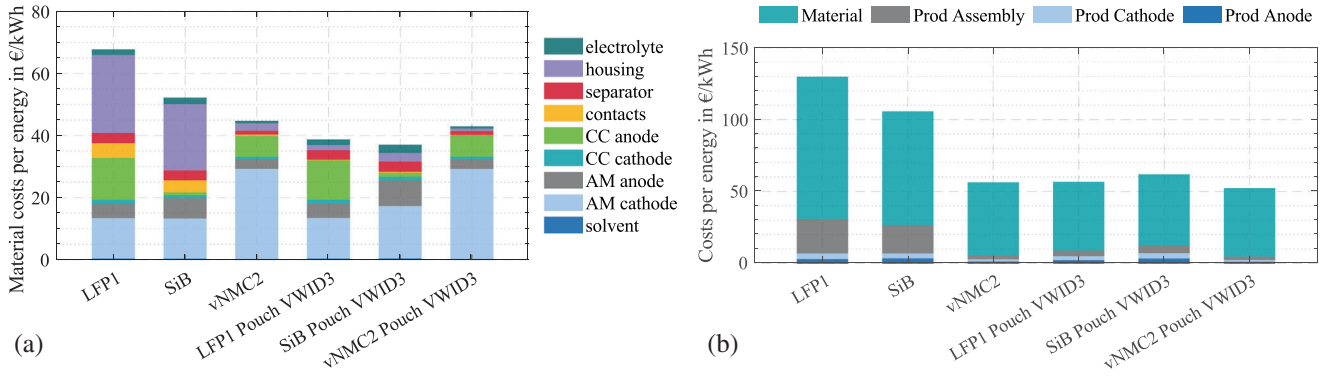

FIGURE 6 | Influence of the housing on the material (a) and total costs (b) per kWh.

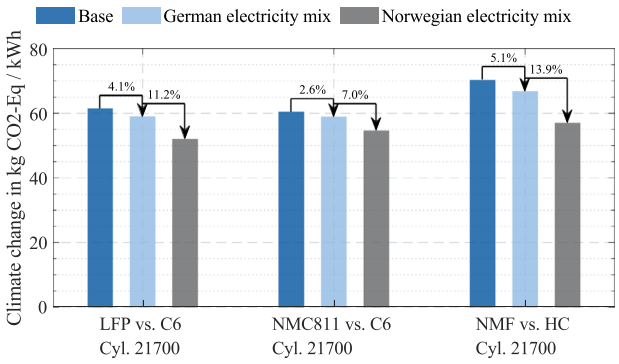

FIGURE 7 | Changes in global warming potential due to different energy mixes.

lower than those of the *SiB* cell when both are fitted into the same housing. Additionally, *vNMC2* emerges as the most economical choice among the three cells due to its lower production costs.

Housing is just one design parameter affecting battery metrics. Variations in electrode designs - such as current collector thickness and electrolyte composition - also play crucial roles. The framework developed in this study enables consistent modeling of battery cells using a common design approach, allowing for the isolation of specific variables for comparative analysis.

3.6 | Sensitivity Regarding the Choice of Energy mix

In Figure 7, the influence of different electricity grid mixes (China, Germany, and Norway) on the GWP is assessed. The generation of the grid mixes was informed by data from the International Energy Agency [93, 94], and their integration into the ecoinvent database was facilitated by the openLCA software. For Germany, the modeled grid mix corresponds to the values reported by the German Environment Agency (UBA) [95]. The resulting specific greenhouse gas emissions amount to 0.626 kg CO_2eq/kWh for China (Base), 0.442 kg CO_2eq/kWh for Germany, and 0.013 kg CO_2eq/kWh for Norway. It is important to note that the scope of the modeling encompasses not only direct electricity generation but also the upstream processes. Therefore, even for Norway, whose electricity supply is entirely based on renewable energies, a non-zero GWP results due to the production of generation infrastructure. In the case of Germany and Norway, the gas provider was adjusted to the European market. It is further important to note that the energy demand within cell production was the only variable altered according to the grid mix. Conversely, upstream energy requirements for material production remained constant, as these components were regarded as purchased parts. The analysis was performed for cells with a cylindrical 21700 housing format, as they exhibit the highest production energy demand per kWh of cell capacity.

The findings indicate that the impact of modifying the grid mix is contingent on the cell chemistry and its concomitant energy density. For NMC811, which exhibits the highest energy density, the GWP decreases by only 2.6 % when moving from China to Germany, and by an additional 7.0 % from Germany to Norway, resulting in a total reduction of about 10.0 % from China to Norway. By contrast, LFP cells exhibit a reduction of approximately 15 %, while sodium-ion cells demonstrate a nearly 20 % reduction. This reflects the lower energy density characteristic of these chemistries: more cells must be produced to provide the functional unit of 1 kWh, thereby amplifying the relative influence of production energy. Results for the remaining impact categories are provided in the S1.

3.7 | Comparison of Model Results with Industrial Developments

The model results show strong consistency with current developments in the battery industry. Overall, the findings confirm that cost, scalability, and application-specific performance remain the primary factors shaping industrial decisions on cell chemistry and design. In terms of environmental performance, the GWP of LFP cells is only slightly higher than that of lithium layered oxide systems (e.g., NMC or NCA). Because no harmonized regulatory framework - such as the forthcoming European battery passport - has yet been implemented, commercial cell manufacturing remains largely cost-driven. As a result, LFP has become the dominant chemistry in large-scale and stationary applications, particularly in China, as it combines low cost with competitive life-cycle performance [96].

LFP also performs clearly better in terms of MRS and acidification potential. Its independence from nickel and cobalt eliminates the reliance on critical materials and reduces the acidifying emissions

of mining and refining. Sodium-ion cells perform best in the case of MRS because they rely on abundant elements such as sodium and iron. However, they are still at an early stage of industrialization. The assumption of the model that sodium-ion cells can be produced in existing lithium-ion lines is technically sound, but not yet realized on scale. Regarding CED, LFP again shows an advantage over layered oxide systems, whose nickel and cobalt processing require significant primary energy. Sodium-ion cells reach comparable CED values in the model, suggesting good future potential once industrial scaling is achieved. Consequently, both the environmental and energy-related results are consistent with observed market developments, where LFP represents the most efficient and scalable chemistry among mature technologies. From an economic perspective, the model confirms that LFP currently offers the lowest production costs among commercial lithium-based cells. Its material and manufacturing costs are considerably lower than those of layered oxide systems and comparable to those projected for sodium-ion batteries. However, sodium-ion technology still lacks mature large-scale production and economies of scale [97, 98]. Industrial choices therefore remain dominated by LFP for cost- and volume-sensitive applications, while high-energy layered oxide chemistries continue to serve performance-oriented markets such as long-range electric vehicles [96]. This split between cost-optimized LFP and performance-oriented NMC/NCA systems in the model directly mirrors the actual market segmentation observed today. The model also reflects current trends in cell format and design. Pouch cells show the lowest GWP and cost [99], while prismatic and cylindrical formats perform similarly. Increasing cell size, for instance, from 21700 to 4680 [34, 100], reduces environmental impacts due to a lower proportion of passive materials, a trend consistent with ongoing industrial development. Larger cells and higher electrode loadings lead to higher energy densities, which are increasingly adopted in practice to enhance material efficiency. In terms of cost, pouch cells perform best overall, but industrial choices remain application-dependent, balancing manufacturability, thermal stability, and mechanical robustness.

4 | Conclusions

This work presents a novel multidimensional framework that integrates electrochemical performance, production costs, and life cycle impacts into a cohesive battery cell assessment. In contrast to prior methods, which were constrained to virtual cells or individual dimensions, the framework facilitates a systematic evaluation of actual commercial cells and their virtual redesigns. It also permits the controlled variation of specific parameters, such as housing or electrode thickness. This capability provides a unique basis for disentangling the influence of individual design choices from confounding effects.

The findings indicate that cathode chemistry and achievable energy density are pivotal factors in determining ecological performance. Sulfate-based precursors have been shown to markedly increase acidification loads. For GWP, layered oxide cathodes with a high nickel content exhibit the lowest values (down to 51.1 kg CO_2-Eq/kWh), mainly due to their high energy density. However, a high nickel share negatively affects acidification, with NMC92 reaching values of up to 1.2 kg SO_2-Eq/kWh. LFP cells, in contrast, can achieve both low GWP values (around 52.9 kg CO_2-Eq/kWh) and simultaneously low acidification levels (around 0.4 kg SO_2-Eq/kWh). LCO demonstrates substandard performance, exhibiting MRS values approximately twice those of NMC/NCA. This is primarily attributable to its high cobalt content and its CED, which is roughly three times higher than for other layered oxide cells due to lower energy density. The findings of the study indicate that the GWP is systematically reduced by higher energy density, thereby underscoring the significance of cell design optimization. The housing type exerts a substantial influence on the outcomes. Pouch cells have been observed to minimize impacts across a wide range of categories, while copper-intensive steel housings are disadvantageous in terms of MRS. Considering only cell level, this might change on module or pack level. SiB cells, on the other hand, reach higher GWP values than LiB cells due to their lower energy density. On the other hand, the use of HC from resin leads to higher impacts compared to natural graphite; this effect would diminish if synthetic graphite were consistently used in LiB anodes.

Beyond the environmental effects, the framework underscores significant cost-performance trade-offs. Cells with increased energy by larger housings or adoption of silicon-doped anodes enable cost savings by economies of scale. SiB and LFP cells achieve the lowest costs in a pouch VW ID3 housing with 31.7 €/kWh and 32.7 €/kWh, respectively. The prices can go up to 82.4 €/kWh (SiB) and 69.3 €/kWh (LFP) in a cylindrical 21700 housing. High nickel results in high capacities but does not necessarily lead to lower cost, as seen for NMC92 which range between 39.6 €/kWh and 62.4 €/kWh.

The integration of systematic parameter variation and integrated cost and LCA analysis establishes a novel foundation for guiding material research and industrial cell development toward more sustainable and economically viable battery technologies. The comparison with industrial developments shows that the modeled environmental, energy, and cost trends closely mirror real-world industry dynamics. The results reproduce key market directions, LFP expansion in cost-driven applications, layered oxides in high-performance segments, and scaling toward larger, more efficient cell formats, thereby confirming the practical relevance and predictive strength of the proposed multidimensional framework.

Acknowledgements

This work was supported by the Federal Ministry for Economic Affairs and Climate Action (BMWK) through the projects finalize! (grant 16EM6001, funding program Renewably Mobile), WINTER (grant 03EI6106D, research initiative Innovations for the Energy Transition), HyFlexBahn (grant 03ETE045A) and Hy-FCD (grant 03EN5027). The authors thank Dominic Peltzer (ISEA) for his contribution to the initial implementation of the method to convert openLCA data into data that Brightway can process.

Open access funding enabled and organized by Projekt DEAL.

Conflicts of Interest

The authors declare no conflict of interest.

Data Availability Statement

The data that support the findings of this study are available in the supplementary material of this article.

References

1. C. Hecht, K. G. Spreuer, J. Figgener, and D. U. Sauer, "Market Review and Technical Properties of Electric Vehicles in Germany,"*Vehicles* 4, no. 4 (2022): 903–916, https://doi.org/10.3390/vehicles4040049.

2. J. Figgener, C. Hecht, D. Haberschusz, et al., "The Development of Battery Storage Systems in Germany: A Market Review (status 2023)", http://arxiv.org/pdf/2203.06762v3.

3. J. Figgener, C. Hecht, H. David, et al., "About Battery Charts", Battery Charts, Accessed December 29, (2025), https://battery-charts.de/battery-charts/.

4. IEA "Global EV Outlook 2021: Accelerating ambitions despite the pandemic, OECD Publishing, Paris", (2021), https://doi.org/10.1787/3a394362-en.

5. K. R. Ngoy, V. T. Lukong, K. O. Yoro, et al., "Lithium-Ion Batteries and the Future of Sustainable Energy: A Comprehensive Review,"*Renewable and Sustainable Energy Reviews* 223 (2025): 115971, https://doi.org/10.1016/j.rser.2025.115971.

6. G. de Carne, S. M. Maroufi, H. Beiranvand, et al., "The Role of Energy Storage Systems for a Secure Energy Supply: A Comprehensive Review of System Needs and Technology Solutions,"*Electric Power Systems Research* 236 (2024): 110963, https://doi.org/10.1016/j.epsr.2024.110963.

7. European Parliament and the Council of the European Union, "Regulation (EU) 2023/1542 of the European Parliament and of the Council of 12 July 2023 concerning batteries and waste batteries, amending Directive 2008/98/EC and Regulation (EU) 2019/1020 and repealing Directive 2006/66/EC," (2023), https://eur-lex.europa.eu/eli/reg/2023/1542/oj.

8. SYSTEMIQ, "Battery Passport Content Guidance: Achieving compliance with the EU Battery Regulation and Increasing Sustainability and Circularity," 2025, https://thebatterypass.eu/wp-content/uploads/qa_content-guidance.pdf.

9. M. Doppelbauer, *Introduction to Electromobility: Technology, Best Practice, Energy and Environment* (Wiesbaden and Heidelberg: Springer, 2024).

10. J. F. Peters, M. Baumann, J. R. Binder, and M. Weil, "On the Environmental Competitiveness of Sodium-Ion Batteries Under a Full Life Cycle Perspective – A Cell-Chemistry Specific Modelling Approach,"*Sustainable Energy & Fuels* 5, no. 24 (2021): 6414–6429, https://doi.org/10.1039/D1SE01292D.

11. S. Zhang, B. Steubing, H. Karlsson Potter, P.-A. Hansson, and Å. Nordberg, "Future Climate Impacts of Sodium-Ion Batteries,"*Resources, Conservation and Recycling* 202 (2024): 107362, https://doi.org/10.1016/j.resconrec.2023.107362.

12. A. Yao, S. M. Benson, and W. C. Chueh, "Critically Assessing Sodium-ion Technology Roadmaps and Scenarios for Techno-Economic Competitiveness Against Lithium-Ion Batteries,"*Nature Energy* 10, no. 3 (2025): 404–416, https://doi.org/10.1038/s41560-024-01701-9.

13. A. K. Prajapati and A. Bhatnagar, "A Review on Anode Materials for Lithium/Sodium-Ion Batteries,"*Journal of Energy Chemistry* 83 (2023): 509–540, https://doi.org/10.1016/j.jechem.2023.04.043.

14. M. Yuan, H. Liu, and F. Ran, "Fast-Charging Cathode Materials for Lithium & Sodium Ion Batteries,"*Materials Today* 63 (2023): 360–379, https://doi.org/10.1016/j.mattod.2023.02.007.

15. M. Kuipers, S. Bihn, M. Junker, and D. U. Sauer, "Development of a Cell Design Environment for Bottom-up Estimation of Performance parameters for Lithium-Ion Batteries and Virtual Cell Design – ISEA Cell & Pack Database (ICPD),"*Journal of Energy Storage* 72 (2023): 108396, https://doi.org/10.1016/j.est.2023.108396.

16. J.-L. Popien, C. Thies, A. Barke, and T. S. Spengler, "Comparative Sustainability Assessment of Lithium-Ion, Lithium-Sulfur, and All-Solid-State Traction Batteries," *The International Journal of Life Cycle Assessment* 28, no. 4 (2023): 462–477, https://doi.org/10.1007/s11367-023-02134-4.

17. G. Wernet, C. Bauer, B. Steubing, J. Reinhard, E. Moreno-Ruiz, and B. Weidema, "The Ecoinvent Database version 3 (part I): Overview and Methodology,"*The International Journal of Life Cycle Assessment* 21, no. 9 (2016): 1218–1230, https://doi.org/10.1007/s11367-016-1087-8.

18. K. W. Knehr, J. J. Kubal, P. A. Nelson, and S. Ahmed, "Battery Performance and Cost Modeling for Electric-Argonne National Laboratory, 5 Version," (2024), https://www.anl.gov/partnerships/batpac-battery-manufacturing-cost-estimation.

19. A. Barke, C. Thies, J.-L. Popien, et al., "Life Cycle Sustainability Assessment of Potential Battery Systems for Electric Aircraft," *Procedia CIRP* 98 (2021): 660–665, https://doi.org/10.1016/j.procir.2021.01.171.

20. M. Chordia, E. Wikner, and A. Nordelöf, "A Model Platform for Solving Lithium-Ion Battery Cell Data Gaps in Life Cycle Assessment, EVS35 Symposium, Oslo 2022," https://www.diva-portal.org/smash/get/diva2:1920443/FULLTEXT01.pdf.

21. F. Degen, M. Mitterfellner, and A. Kampker, "Comparative Life Cycle Assessment of Lithium–Ion, Sodium–Ion, and Solid–State Battery Cells for Electric Vehicles,"*Journal of Industrial Ecology*, 29, 1, (2024): 113–128, https://doi.org/10.1111/jiec.13594.

22. M. Lechner, A. Kollenda, K. Bendzuck, et al., "Cost Modeling for the GWh-Scale Production of Modern Lithium-Ion Battery Cells,"*Communications Engineering* 3, no. 1 (2024): 155, https://doi.org/10.1038/s44172-024-00306-0.

23. S. Orangi, N. Manjong, D. P. Clos, L. Usai, O. S. Burheim, and A. H. Strømman, "Historical and Prospective Lithium-Ion Battery Cost Trajectories from a Bottom-up Production Modeling Perspective,"*Journal of Energy Storage* 76 (2024): 109800, https://doi.org/10.1016/j.est.2023.109800.

24. F. Duffner, M. Wentker, M. Greenwood, and J. Leker, "Battery cost modeling: A Review and Directions for Future Research,"*Renewable and Sustainable Energy Reviews* 127 (2020): 109872, https://doi.org/10.1016/j.rser.2020.109872.

25. Institute for Power Electronics and Electrical Drives (RWTH Aachen University), "ISEA Cell and Pack Database," (2024), GitHub repository, https://git.rwth-aachen.de/isea/isea-cell-and-pack-database.

26. M. F. Börner, "Ein prozessbasiertes Modell zur Berechnung der Kosten von Lithium-Ionen-Batteriezellen," (Aachen: Institut fuer Stromrichtertechnik und Elektrische Antriebe, 2024).

27. ecoinvent, "ecoinvent v3.11 ecoinvent", Accessed September 11, (2025): https://ecoinvent.org/ecoinvent-v3-11/.

28. Y. Xiong, H. Xing, Y. Fan, et al., "SiO x -based Graphite Composite Anode and Efficient Binders: Practical Applications in Lithium-Ion Batteries," *RSC Advances* 11, no. 14 (2021): 7801–7807, https://doi.org/10.1039/d0ra10283k.

29. J. Schmalstieg, C. Rahe, M. Ecker, and D. U. Sauer, "Full Cell Parameterization of a High-Power Lithium-Ion Battery for a Physico-Chemical Model: Part I. Physical and Electrochemical Parameters,"*Journal of The Electrochemical Society* 165, no. 16 (2018): A3799–A3810, https://doi.org/10.1149/2.0321816jes.

30. J. Schmalstieg and D. U. Sauer, "Full Cell Parameterization of a High-Power Lithium-Ion Battery for a Physico-Chemical Model: Part II. Thermal Parameters and Validation,"*Journal of The Electrochemical Society* 165, no. 16 (2018): A3811–A3819, https://doi.org/10.1149/2.0331816jes.

31. M. Schütte, H. Laufen, D. Luder, et al., "First Full Cell Parameterization of a Commercial Layered Oxide/Hard Carbon Sodium-Ion 18650 Battery Cell for a Physico-Chemical Model,"*Journal of Energy Storage* 107 (2025): 114931, https://doi.org/10.1016/j.est.2024.114931.

32. L. Wildfeuer, N. Wassiliadis, A. Karger, F. Bauer, and M. Lienkamp, "Teardown Analysis and Characterization of a Commercial Lithium-Ion Battery for Advanced Algorithms in Battery Electric Vehicles,"*Journal of Energy Storage* 48 (2022): 103909, https://doi.org/10.1016/j.est.2021.103909.

33. S. Stock, J. Hagemeister, S. Grabmann, et al., "Cell Teardown and Characterization of an Automotive Prismatic LFP Battery,"*Electrochimica Acta* 471 (2023): 143341, https://doi.org/10.1016/j.electacta.2023.143341.

34. M. Ank, A. Sommer, K. Abo Gamra, et al., "Lithium-Ion Cells in Automotive Applications: Tesla 4680 Cylindrical Cell Teardown and Characterization,"*Journal of The Electrochemical Society* 170, no. 12 (2023): 120536, https://doi.org/10.1149/1945-7111/ad14d0.

35. M. Ecker, T. K. D. Tran, P. Dechent, S. Käbitz, A. Warnecke, and D. U. Sauer, "Parameterization of a Physico-Chemical Model of a Lithium-Ion Battery,"*Journal of The Electrochemical Society* 162, no. 9 (2015): A1836–A1848, https://doi.org/10.1149/2.0551509jes.

36. T. Furukawa, Y. Hirakawa, H. Kondo, T. Kanemura, and E. Wakai, "Chemical Reaction of Lithium with Room Temperature Atmosphere of Various Humidities,"*Fusion Engineering and Design* 98–99 (2015): 2138–2141, https://doi.org/10.1016/j.fusengdes.2014.11.019.

37. A. Jain, S. P. Ong, G. Hautier, et al., "Commentary: The Materials Project: A Materials Genome Approach to Accelerating Materials Innovation,"*APL Materials* 1, no. 1 (2013), https://doi.org/10.1063/1.4812323.

38. D. Andre, S.-J. Kim, P. Lamp, et al., "Future Generations of Cathode Materials: An Automotive Industry Perspective,"*Journal of Materials Chemistry A* 3, no. 13 (2015): 6709–6732, https://doi.org/10.1039/C5TA00361J.

39. D. Andre, H. Hain, P. Lamp, F. Maglia, and B. Stiaszny, "Future High-Energy Density Anode Materials from an Automotive Application Perspective,"*Journal of Materials Chemistry A* 5, no. 33 (2017): 17174–17198, https://doi.org/10.1039/C7TA03108D.

40. N. Nitta, F. Wu, J. T. Lee, and G. Yushin, "Li-Ion Battery Materials: Present and Future,"*Materials Today* 18, no. 5 (2015): 252–264, https://doi.org/10.1016/j.mattod.2014.10.040.

41. T. Fan, Y. Wang, V. K. Harika, et al., "Highly Stable 4.6 V LiCoO2 Cathodes for Rechargeable Li Batteries by Rubidium-Based Surface Modifications,"*Advanced Science (Weinheim, Baden-Wurttemberg, Germany)* 9, no. 33 (2022): e2202627, https://doi.org/10.1002/advs.202202627.

42. C. Lim, B. Yan, H. Kang, et al., "Analysis of Geometric and Electrochemical Characteristics of Lithium Cobalt Oxide Electrode with Different Packing Densities,"*Journal of Power Sources* 328 (2016): 46–55, https://doi.org/10.1016/j.jpowsour.2016.07.119.

43. I. Cho, J. Choi, K. Kim, M.-H. Ryou, and Y. M. Lee, "A Comparative Investigation of Carbon Black (Super-P) and Vapor-Grown Carbon Fibers (VGCFs) as Conductive Additives for Lithium-Ion Battery Cathodes,"*RSC Advances* 5, no. 115 (2015): 95073–95078, https://doi.org/10.1039/C5RA19056H.

44. Y. Son, H. Cha, C. Jo, et al., "Reliable Protocols for Calculating the Specific Energy and Energy Density of Li-Ion Batteries,"*Materials Today Energy* 21 (2021): 100838, https://doi.org/10.1016/j.mtener.2021.100838.

45. M. Doyle and Y. Fuentes, "Computer Simulations of a Lithium-Ion Polymer Battery and Implications for Higher Capacity Next-Generation Battery Designs,"*Journal of The Electrochemical Society* 150, no. 6 (2003): A706, https://doi.org/10.1149/1.1569478.

46. J. Sturm, A. Rheinfeld, I. Zilberman, et al., "Modeling and Simulation of Inhomogeneities in a 18650 Nickel-Rich, Silicon-Graphite Lithium-Ion Cell during Fast Charging,"*Journal of Power Sources* 412 (2019): 204–223, https://doi.org/10.1016/j.jpowsour.2018.11.043.

47. W. Li, Y. Qin, S. Lin, et al., "Active Material Blending Strategy Improves the Comprehensive Performance of Electrode: A Case Study,"*Journal of Power Sources* 631 (2025): 236275, https://doi.org/10.1016/j.jpowsour.2025.236275.

48. MTI Corporation, "Hard Carbon Single-Side Coated Al Foil for Sodium-Ion Battery Anode (241 L x 200 W x 0.09 Thickness mm) 5 Sheets/Bag - BCAF-BHCSS, MTI Corporation," Accessed December 29, (2025), https://mtixtl.com/en-euea/products/hard-carbon-single-side-coated-al-foil-for-sodium-ion-battery-anode-241-l-x-200-w-x-0-09-thickness-mm-5-sheets-bag-bcaf-bhcss?_pos=1&_sid=2ee8d2d4b&_ss=r.

49. MTI Corporation, "Single-Side Coated Layered Oxide NaNi1/3Fe1/3Mn1/3O2 for Sodium-Ion Battery Cathode (241 L x 200 W x 0.08 Thickness mm) 5 Sheets/Bag - BCAF-NFMOSS, MTI Corporation," Accessed December 29, 2025, https://mtixtl.com/en-euea/products/bcaf-nfmoss?_pos=1&_sid=268f32f51&_ss=r.

50. J. Gorsch, J. Schneiders, M. Frieges, et al., "Contrasting a BYD Blade Prismatic Cell and Tesla 4680 Cylindrical Cell with a Teardown Analysis of Design and Performance,"*Cell Reports Physical Science* 6, no. 3 (2025): 102453, https://doi.org/10.1016/j.xcrp.2025.102453.

51. iEST, "Blade Cell Expansion Testing: Insights for Blade Battery Technology and Design iEST, August 21,", (2025), https://iestbattery.com/case/blade-batteries-expansion-behavior.

52. F. J. Günter and N. Wassiliadis, "State of the Art of Lithium-Ion Pouch Cells in Automotive Applications: Cell Teardown and Characterization,"*Journal of The Electrochemical Society* 169, no. 3 (2022): 030515, https://doi.org/10.1149/1945-7111/ac4e11.

53. N. Wassiliadis, M. Steinsträter, M. Schreiber, et al., "Quantifying the State of the Art of Electric Powertrains in Battery Electric Vehicles: Range, Efficiency, and Lifetime from Component to System Level of the Volkswagen ID.3,"*eTransportation* 12 (2022): 100167, https://doi.org/10.1016/j.etran.2022.100167.

54. M. Lain and E. Kendrick, "Understanding the Limitations of Lithium-Ion Batteries at High Rates,"*Journal of Power Sources* 493 (2021): 229690, https://doi.org/10.1016/j.jpowsour.2021.229690.

55. M. J. Lain, J. Brandon, and E. Kendrick, "Design Strategies for High Power vs. High Energy Lithium-Ion Cells,"*Batteries* 5, no. 4 (2019): 64, https://doi.org/10.3390/batteries5040064.

56. R. Tao, Y. Gu, Z. Du, X. Lyu, and J. Li, "Advanced Electrode Processing for Lithium-Ion Battery Manufacturing,"*Nature Reviews Clean Technology* 1, no. 2 (2025): 116–131, https://doi.org/10.1038/s44359-024-00018-w.

57. M. Greenwood, M. Wentker, and J. Leker, "A Bottom-Up Performance and Cost Assessment of Lithium-Ion Battery Pouch Cells Utilizing Nickel-Rich Cathode Active Materials and Silicon-Graphite Composite Anodes,"*Journal of Power Sources Advances* 9 (2021): 100055, https://doi.org/10.1016/j.powera.2021.100055.

58. M. Fakhrudin and E. Kartini, "NMC Cathode Precursor Synthesis by Hydroxide Co-Precipitation Method: A Mini Review,"*AIP Conference Proceedings* 2932, no. 1 (2023): 020007, https://doi.org/10.1063/5.0174823.

59. R. Jain, S. Kumar, and S. K. Meena, "Precipitating Agent (NaOH and NH4OH) Dependent Magnetic Properties of Cobalt Ferrite Nanoparticles,"*AIP Advances* 12, no. 9 (2022), https://doi.org/10.1063/5.0098157.

60. A. Kim, W. B. Portner, C. Mutel, D. de Koning, J. Gonçalves, and T. Diepers, "Brightway LCA Software Framework GitHub repository", (2025), https://github.com/brightway-lca.

61. C. Mutel, "Brightway: An open source framework for Life Cycle Assessment,"*The Journal of Open Source Software* 2, no. 12 (2017): 236, https://doi.org/10.21105/joss.00236.

62. greendelta, "Toolbar: Tools - openLCA 2 manual", (2025), https://greendelta.github.io/openLCA2-manual/running_olca/toolbar_tools.html?highlight=ipc#toolbar-tools.

63. U.S. Energy Information Administration, "China Dominates Global Trade of Battery Minerals - U.S. Energy Information Administration (EIA)", (2025), https://www.eia.gov/todayinenergy/detail.php?id=65305.

64. C. François, "Presentation of OpenLCA2BW Package, LCA Data Transfer from OpenLCA to Brightway2", (2022), https://hal-emse.ccsd.cnrs.fr/emse-04453517.

65. R. Heijungs and M. A. J. Huijbregts, "A Review of Approaches to Treat Uncertainty in LCA," *International Congress on Environmental Modelling and Software* (2004), https://scholarsarchive.byu.edu/iemssconference/2004/all/197/.

66. R. K. Rosenbaum, S. Georgiadis, and P. Fantke, "Uncertainty Management and Sensitivity Analysis," In *Life Cycle Assessment*, eds. M. Z. Hauschild, R. Rosenbaum, and S. I. Olsen, 271–321 (Cham: Springer, 2018), ISBN 978-3-319-56475-3, https://link.springer.com/chapter/10.1007/978-3-319-56475-3_11.

67. A. Krotov, G. Karuna, S. Bhattaru, et al., "Life Cycle Assessment of Biofuels Using Monte Carlo Simulation,"*E3S Web of Conferences* 581 (2024): 01002, https://doi.org/10.1051/e3sconf/202458101002.

68. M. A. J. Huijbregts, "Application of Uncertainty and Variability in LCA," *The International Journal of Life Cycle Assessment* 3, no. 5 (1998): 273–280, https://doi.org/10.1007/BF02979835.

69. N. Adams and K. Allacker, "Parameter Sensitivity and Data Uncertainty Assessment of the Cradle-to-Gate Environmental Impact of State-of-the-Art Passive Daytime Radiative Cooling Materials,"*Environmental Sciences Europe* 37, no. 1 (2025): 1–18, https://doi.org/10.1186/s12302-025-01093-x.

70. ISO 14040, "Environmental Management - Life Cycle Assessment - Principles and Framework", (2006), https://www.iso.org/standard/37456.html.

71. X. Lai, Q. Chen, X. Tang, et al., "Critical Review of Life Cycle Assessment of Lithium-Ion Batteries for Electric Vehicles: A Lifespan Perspective,"*eTransportation* 12 (2022): 100169, https://doi.org/10.1016/j.etran.2022.100169.

72. Z. Quist, "Life Cycle Assessment (LCA) - Everything You Need to Know,"*Ecochain LCA Software*, https://ecochain.com/blog/life-cycle-assessment-lca-guide/.

73. G. Finnveden and J. Potting, "Life Cycle Assessment," *Encyclopedia of Toxicology: Third Edition* (2014): 74–77, https://doi.org/10.1016/B978-0-12-386454-3.00627-8.

74. K. Rüdele and M. Wolf, "Grave Without Death? A Plea for a More Accurate Wording of Study Scopes,"*The International Journal of Life Cycle Assessment* 28, no. 9 (2023): 1073–1077, https://doi.org/10.1007/s11367-023-02208-3.

75. D. Gürzenich, J. Mathur, N. K. Bansal, and H.-J. Wagner, "Cumulative Energy Demand for Selected Renewable Energy Technologies,"*The International Journal of Life Cycle Assessment* 4, no. 3 (1999): 143–149, https://doi.org/10.1007/BF02979448.

76. M. A. J. Huijbregts, Z. J. N. Steinmann, P. M. F. Elshout, et al., "ReCiPe2016: A Harmonised Life Cycle Impact Assessment Method at Midpoint and Endpoint Level,"*The International Journal of Life Cycle Assessment* 22, no. 2 (2017): 138–147, https://doi.org/10.1007/s11367-016-1246-y.

77. PRé Sustainability, "ReCiPe: Life Cycle Assessment," (2016), https://pre-sustainability.com/articles/recipe/.

78. N. B. Manjong, L. Usai, S. Orangi, D. P. Clos, and A. H. Strømman, "Exploring Raw Material Contributions to the Greenhouse Gas Emissions of Lithium-Ion Battery Production,"*Journal of Energy Storage* 100 (2024): 113566, https://doi.org/10.1016/j.est.2024.113566.

79. T. Zhang, Y. Bai, X. Shen, et al., "Cradle-to-Gate Life Cycle Assessment of Cobalt Sulfate Production Derived from a Nickel–Copper–Cobalt Mine in China,"*The International Journal of Life Cycle Assessment* 26, no. 6 (2021): 1198–1210, https://doi.org/10.1007/s11367-021-01925-x.

80. J. C. Kelly, M. Wang, Q. Dai, and O. Winjobi, "Energy, Greenhouse Gas, and Water Life Cycle Analysis of Lithium Carbonate and Lithium Hydroxide Monohydrate from Brine and Ore Resources and Their Use in Lithium-Ion Battery Cathodes and Lithium-Ion Batteries,"*Resources, Conservation and Recycling* 174 (2021): 105762, https://doi.org/10.1016/j.resconrec.2021.105762.

81. TheGlobalEconomy, "China Electricity Imports - Data, Chart," https://www.theglobaleconomy.com/China/electricity_imports/.

82. International Energy Agency, "China - Countries & Regions - IEA," (2025), https://www.iea.org/countries/china/electricity.

83. K. H. Choi and G. Azimi, "Crystallization of Nickel Sulfate and Its Purification Process: Towards Efficient Production of Nickel-Rich Cathode Materials for Lithium-Ion Batteries,"*RSC Advances* 13, no. 41 (2023): 28501–28512, https://doi.org/10.1039/D3RA04280D.

84. B. Han, O. Bøckman, B. P. Wilson, M. Lundström, and M. Louhi-Kultanen, "Purification of Nickel Sulfate by Batch Cooling Crystallization,"*Chemical Engineering & Technology* 42, no. 7 (2019): 1475–1480, https://doi.org/10.1002/ceat.201800695.

85. K. H. Choi, J. Jang, S. Bedrossian, and G. Azimi, "Impact of Impurities on Nickel Sulfate Crystallization and Strategies for Removal: Advancing Toward Battery-Grade Nickel Sulfate Production,"*Industrial & Engineering Chemistry Research* 64, no. 8 (2025): 4227–4249, https://doi.org/10.1021/acs.iecr.4c03711.

86. ecoinvent, ecoQuery, "cobalt production - Global - nickel sulfate," (2025), https://ecoquery.ecoinvent.org/3.11/cutoff/dataset/23578/documentation.

87. S. Wickerts, R. Arvidsson, A. Nordelöf, M. Svanström, and P. Johansson, "Prospective life cycle assessment of sodium–ion batteries made from abundant elements,"*Journal of Industrial Ecology* 28, no. 1 (2024): 116–129, https://doi.org/10.1111/jiec.13452.

88. C. M. Julien and A. Mauger, "Fabrication of $Li_4Ti_5O_{12}$ (LTO) as Anode Material for Li-Ion Batteries,"*Micromachines* 15, no. 3 (2024), https://doi.org/10.3390/mi15030310.

89. J. B. Dunn, C. James, L. Gaines, K. Gallagher, Q. Dai, and J. C. Kelly, "Material and Energy Flows in the Production of Cathode and Anode Materials for Lithium Ion Batteries," (2015), https://doi.org/10.2172/1224963.

90. G. Wang, H. Wang, G. Ma, et al., "Investigation on process mechanism of a novel energy-saving synthesis for high performance $Li_4Ti_5O_{12}$ anode material,"*Journal of Energy Chemistry* 70 (2022): 266–275, https://doi.org/10.1016/j.jechem.2022.02.056.

91. Q. Dai, J. C. Kelly, L. Gaines, and M. Wang, "Life Cycle Analysis of Lithium-Ion Batteries for Automotive Applications,"*Batteries* 5, no. 2 (2019): 48, https://doi.org/10.3390/batteries5020048.

92. European Commission, "Critical raw materials," (2025), https://single-market-economy.ec.europa.eu/sectors/raw-materials/areas-specific-interest/critical-raw-materials_en.

93. International Energy Agency, "Germany – Countries & Regions – IEA," (2025), https://www.iea.org/countries/germany/electricity.

94. International Energy Agency, "Norway – Countries & Regions – IEA," (2025), https://www.iea.org/countries/norway/electricity.

95. P. Icha, T. Lauf, "Entwicklung der spezifischen Treibhausgas-Emissionen des deutschen Strommix in den Jahren 1990–2024," *Umweltbundesamt* (2025), https://doi.org/10.60810/openumwelt-7844.

96. Goldman Sachs, "Electric Vehicle Battery Prices are Expected to Fall Almost 50% by 2026," (2024), https://www.goldmansachs.com/insights/articles/electric-vehicle-battery-prices-are-expected-to-fall-almost-50-percent-by-2025.

97. P. Phogat, S. Rawat, S. Dey, and M. Wan, "Advancements and Challenges in Sodium-ion Batteries: A Comprehensive Review of Materials, Mechanisms, and Future Directions for Sustainable Energy Storage,"*Journal of Alloys and Compounds* 1020 (2025): 179544, https://doi.org/10.1016/j.jallcom.2025.179544.

98. X. Cai, Y. Yue, Z. Yi, J. Liu, Y. Sheng, and Y. Lu, "Challenges and Industrial Perspectives on the Development of Sodium Ion Batteries,"*Nano Energy* 129 (2024): 110052, https://doi.org/10.1016/j.nanoen.2024.110052.

99. A. Epp, R. Wendland, J. Behrendt, R. Gerlach, and D. U. Sauer, "Holistic Battery System Design Optimization for Electric Vehicles using a Multiphysically Coupled Lithium-Ion Battery Design Tool," *Journal of Energy Storage* 52 (2022): 104854, https://doi.org/10.1016/j.est.2022.104854.

100. A. Epp and D. U. Sauer, "Multiperspective Optimization of Cell and Module Dimensioning for Different Lithium–Ion Cell Formats on Geometric and Generic Assumptions," *Energy Technology* 10, no. 3 (2022): 2100874, https://doi.org/10.1002/ente.202100874.

Supporting Information

Additional supporting information can be found online in the Supporting Information section.

Supporting File: aenm70441-sup-0001-SuppMat.pdf

Supporting File: aenm70441-sup-0002-Data.zip